DUAL-SPECTRAL ENDOSCOPIC NEAR-INFRARED OPTICAL TOMOGRAPHY FOR ASSESSMENT OF HEMOGLOBIN CONCENTRATION AND OXYGEN SATURATION

By

Hao Xie

Bachelor of Science in Electrical Engineering

North China Electrical Power University

Beijing, China

1997

Submitted to the Faculty of the
Graduate College of the
Oklahoma State University
in partial fulfillment of
the requirements for
the Degree of
MASTER OF SCIENCE
July, 2008

DUAL-SPECTRAL ENDOSCOPIC NEAR-INFRARED OPTICAL TOMOGRAPHY FOR ASSESSMENT OF HEMOGLOBIN CONCENTRATION AND OXYGEN SATURATION

Thesis Approved:

Dr. Daqing Piao

Thesis Adviser

Dr. Charles F. Bunting

Dr. Weili Zhang

Dr. Jerzy Krasinski

Dr. A.Gordon Emslie

Dean of the Graduate College

TABLE OF CONTENTS

Chapter Page

LIST OF FIGURES

CHAPTER 1

INTRODUCTION

1.1 Motivation

Prostate cancer is a disease which develops in the prostate, a small internal gland in the male reproductive system. It is a very common type of cancer in men in the United States, where it is responsible for many male deaths. Figure 1.1 (a) and (b) shows the prostate anatomy and comparison between normal and cancerous prostate. Rates of prostate cancer vary widely across the world. According to the World Health Organization, there were 679,023 new cases and 221,002 deaths from prostate cancer worldwide in 2002; in 2004, prostate cancer was estimated to account for 198,100 cases and 31,500deaths in the USA. [1]

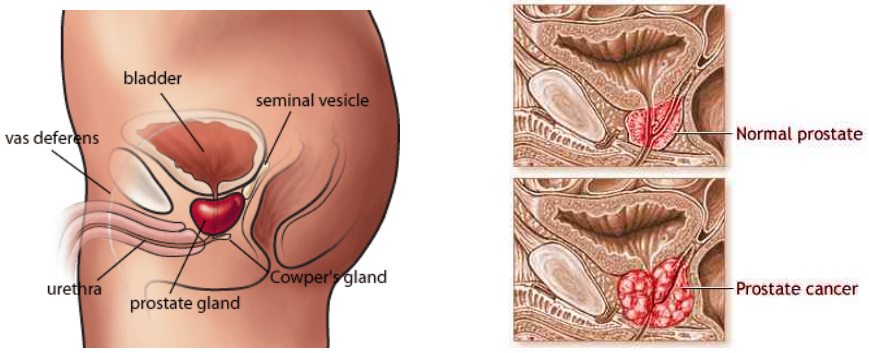

(a) Size and Position of Prostate (B) Normal and Cancerous Prostate

Figure 1.1. Normal and Cancerous Prostate

Many people who develop prostate cancer never have any symptoms and most cases of prostate cancer are discovered by physical examination or by screening blood tests of prostate specific antigen (PSA). The suspected prostate cancer is then confirmed by biopsy. Prostate biopsy is a procedure in which small samples are removed from prostate under ultrasound (US) guidance for microscope examination to confirm and grade the cancer. Unfortunately, the prostate biopsy suffers low accuracy because the samples of the prostate may not be obtained from the right position of the tumor due to the lack of specificity in US guidance. Under this circumstance, auxiliary imaging method is needed to guide the biopsy needle to the correct target area.

1.2 Methodology

Near-infrared diffuse optical tomography (NIR-DOT) is an alternative method which can be used to image physiologic parameters of biological tissue in-vivo. As a unique and interesting optical imaging modality, NIR-DOT has been developed continuously over the past decades, and many imaging systems have been designed for use in experimental studies and clinical trials. It has emerged possibly due to two principal areas of technological development, i.e. NIR instrumentation and capabilities for diffuse image reconstruction. Advances in instrumentation have enabled multi-wavelength measurements from time-domain or frequency domain based systems to be obtained with percent noise established around 1%. [2] In addition, model-based reconstruction schemes have allowed the field to obtain concentrations of tissue chromophors and scatter-based parameters.

In NIR-DOT, near infrared light is absorbed and scattered when it transport through

the tissue. As shown in Figure 1.2, at near infrared window (700 – 900 nm) of light wavelength, the absorption coefficient of the water is very low; the absorption coefficient of the hemoglobin is higher than the water, but it is still relatively low. This characteristic allows near-infrared light penetrate through a few centimeters of human tissue and the scattering becomes the dominant interaction than absorption. Therefore, the NIR-DOT can provide very high intrinsic contrast images (from the different absorption coefficient of the tissue); meanwhile it suffers relative lower resolution. [3]

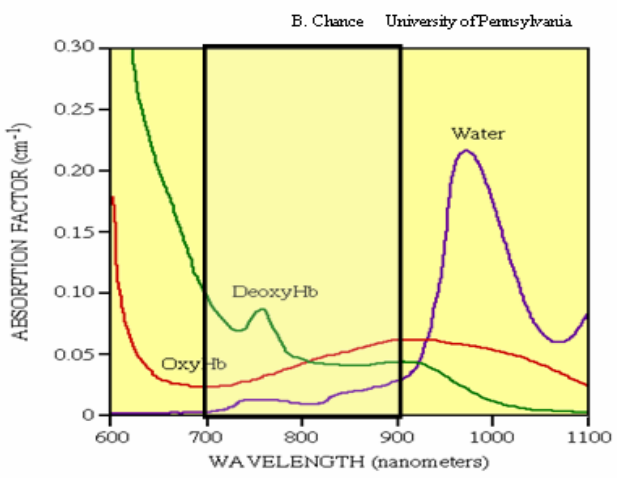

Figure 1.2. Absorption Coefficients of Hemoglobin and Water.

Today, application of NIR-DOT has been developed in many different areas such as animal tomography, neonate brain tomography, female breast tomography and transrectal tomography. NIR-DOT can provide functional information for tumor because the vascular density and hence the hemoglobin concentration and the oxygen saturation level are different between tumor and normal tissue. [4] For example, medical studies have shown that when female breast cancer occurs, the degree of vascularity in tumors will increase dramatically. As a result, there is an elevated hemoglobin content and hence high intrinsic optical contrast between tumor and normal tissue. [5]

Similarly, for prostate cancer detection, NIR-DOT is expected to give functional information and improve the accuracy of the prostate biopsy. However, due to the anatomy of the prostate, regular NIR-DOT needs to be transferred into endoscopic mode. This is a novel non-invasive technique that allows the measurement of blood-based intrinsic optical contrast to be achieved for cancer detection in internal organs. Furthermore, based on the different optical absorption coefficients of the oxygenated and deoxygenated hemoglobin in the near infrared band, one can quantify the total hemoglobin concentration and the oxygen saturation of the blood with dual-spectral near-infrared diffuse optical tomography. So it is necessary to implement dual-spectral detection to endoscopic NIR tomography to assess the hemoglobin concentration and oxygenation levels in internal organs such as prostate. [6]

In this thesis, a dual-spectral band endoscopic NIR tomography system will be presented. Two superluminescent diode (SLD) light sources (Superlum Inc.) having 14nm bandwidth centered at 780nm and 830nm were used as the source. The two wavelengths were considered due to the different optical properties of oxygenated and deoxygenated hemoglobin at the near-infrared window. Then the collimated beams from two SLD sources were launched onto a grating at different incident angles such that the diffraction angles were identical. The overlapped linear dispersion of the source spectra were then collimated and coupled to a linear fiber bundle to create a spread-spectral-encoding of each wavelength band onto the array of fibers, allowing parallel delivery of a separate pair of wavelengths into each fiber of the endoscopic NIR probe. The source fibers and detector fibers in the probe were arranged in a circular array for endoscopic transverse imaging by use of a cone prism for 90 degree light deflection.

The detected light signal was spectrally-decoded by a spectrometer, and the dual-band signals corresponding to all source-detector channels were acquired simultaneously using a CCD camera for tomographic reconstruction of absorption contrast in both spectral bands. [7]

CHAPTER 2

MATHEMATICAL THEORY

This chapter explains the mathematical theory of the near-infrared diffuse optical tomography (NIR-DOT) and the mode-based image reconstruction algorithm.

2.1 Near Infrared Diffuse Optical Tomography

Near-infrared (NIR) optical tomography has been demonstrated as a non-invasive diagnostic imaging technique for many years. As mentioned earlier, at near infrared window (700 – 900 nm) of light wavelength, the water absorption of human tissue is pretty low (compare with the hemoglobin) to allow light penetration through a few centimeters of tissue. When near-infrared light passes through the human tissue, we can obtain two types of optical properties for human tissue: the absorption coefficient and reduced scattering coefficient. These two parameters specify a photon's probability of absorption or scattering per unit distance traveled. The absorption of the tissue is related to the concentration of the main chromophors present in the tissue such as hemoglobin and water. The scattering is related to the scatter size and number density.

For near-infrared light, the human tissue is a turbid media which has lower absorption coefficient and strong scattering coefficient. This type of light diffusion is characterized by elastic processes resulting from refractive index fluctuations at the

microscopic level of cellular organelles and is quite complicated. Due to this reason, image reconstruction in near infrared imaging becomes a challenging problem.

2.2 Theory Background

Image reconstruction is an inverse problem. In optical imaging, the inverse problem involves finding the distribution of optical parameters in tissue through surface measurement. To solve inverse problem, the corresponding forward problem needs to be solved at the first step to construct a model for light transport that can be used to calculate the measurement datasets on the boundary.

Generally, the Boltzman transport equation can be used to describe the propagation of light in turbid media. The time domain Boltzman transport equations are: [8]

$$\frac{1}{c_m}\frac{\partial L(r,t,\hat{s})}{\partial t}+\nabla\cdot\hat{s}L(r,t,\hat{s})=-\mu_t L(r,t,\hat{s})+\mu_s\iint_{4\pi}L(r,t,\hat{s})f(\hat{s},\hat{s}')d\Omega'+S(r,t,\hat{s}) \tag{2.2.1}$$

Here $L(r,t,\hat{s})$ is the radiance at point r, time t and solid angle $\hat{s}$; c_m is the velocity of light in the medium; μ_a is the absorption coefficient and μ_s is the scattering coefficient, and $\mu_t=\mu_a+\mu_s$. $f(\hat{s},\hat{s}')$ is the normalized differential scattering function, which predicts the probability of scattering from angle $\hat{s}'$ into the angle $\hat{s}$; $S(r,t,\hat{s})$ is the source function.

The sum of a complex photon isotropic fluence $\Phi(r,t)=\iint_{4\pi}L(r,t,\hat{s})d\Omega$ and a small directional flux $J(r,t)=\iint_{4\pi}L(r,t,\hat{s})\hat{s}d\Omega$ is used to represent the radiance in human tissue; then the radiance at given point can be expressed by the Radiative Transfer Equation

(RTE):

$$L(r,t,\hat{s}) = \frac{1}{4\pi}\Phi(r,t) + \frac{3}{4\pi}J(r,t)\cdot\hat{s} \tag{2.2.2}$$

When integrating over all angles of the radiation transport equation, we can arrive at the continuity equation for the photon flux:

$$\frac{1}{c_m}\frac{\partial\Phi(r,t,\hat{s})}{\partial t} + \nabla\cdot J(r,t,\hat{s}) = -\mu_a\Phi(r,t,\hat{s}) + S_0(r,t) \tag{2.2.3}$$

By Fick's Law: $J(r,t) = -k\nabla\Phi(r,t)$, where $k = \frac{1}{3(\mu_a + \mu_s')}$ is the diffusion coefficient and $\mu_s' = (1-g)\mu_s$, the time domain diffusion equation can be expressed as follows:

$$\frac{1}{c_m}\frac{\partial\Phi(r,t)}{\partial t} - \nabla\cdot k\nabla\Phi(r,t) + \mu_a\Phi(r,t) = S_0(r,t) \tag{2.2.4}$$

The frequency-domain version can be calculated by Fourier transformation:

$$-\nabla\cdot k\nabla\Phi(r,\omega) + \left(\mu_a + \frac{i\omega}{c_m}\right)\Phi(r,\omega) = S_0(r,\omega) \tag{2.2.5}$$

Here $Q_0(r,\omega)$ is an isotropic source; $\Phi_0(r,\omega)$ is the complex photon fluence arising from the intensity modulated part of the source; ω is the modulation frequency. [8][9]

At the measurement site r, the outward directed flux (the so-called complex exitance, which means the total light which comes off a surface, dependent on the illuminance on and the reflectance of the surface) is calculated as

$$\hat{\Gamma}(r,\omega) = -\kappa(r)\hat{n}\bullet\nabla\Phi(r,\omega) \tag{2.2.6}$$

Here $\hat{n}$ is the outward-pointing normal to the boundary. Then the complex exitance is used to obtain the measurable quantities of the photon density wave which includes the

amplitude $A(r,\omega)=\left|\hat{\Gamma}(r,\omega)\right|$ and the phase angle $\varphi(r,\omega)=\arg\hat{\Gamma}(r,\omega)$.

For the boundary condition, Robin boundary condition, which can be derived from the assumption that the total inward directed energy current at the boundary is zero, is introduced as:

$$\Phi(r,\omega)+2\kappa(r)\hat{n}\bullet\nabla\Phi(r,\omega)=0 \qquad (2.2.7)$$

As mentioned above, the light source is modeled as an isotropic point source at a depth of $\frac{1}{u_s'}$ below the surface of the medium. [10][11][12] [13][14]

2.3 Reconstruction Algorithm

Based on linearization and iteration, many methods can address the inverse problem. A common method is presented in this summary.

The solution of the inverse problem can be treated as a minimization problem. Levenberg-Marquardt algorithm can be used to estimate the nonlinear parameters for image reconstruction. It is to minimize the objective function which depends on the estimation data Φ^c (calculated by forward model) and the measured data Φ^m that includes the position of source and detector, operating frequency and spatial distribution of μ_a and μ_s'.

Levenberg-Marquardt algorithm is typically expressed as:

$$\Psi = X^2 = \sum_{i=1}^{N_m}\left(\Phi_i^c-\Phi_i^m\right)^2 = \left\|\Phi^c(x)-\Phi^m\right\|_2^2 = \left[\Phi^c(x)-\Phi^m\right]^T\left[\Phi^c(x)-\Phi^m\right] \qquad (2.3.1)$$

where i is the index for each source-detector pair and N_m is the total number of measurements. X is the vector of unknown parameter $x=\left[\mu_a(\lambda), D(\lambda)\right]^T$, and then the

derivative of ψ could be expressed as:

$$\Psi'(x) = \frac{d\left[\Phi^c(x) - \Phi^m\right]^T \left[\Phi^c(x) - \Phi^m\right]}{dx} = -2J^T b \tag{2.3.2}$$

Here J is a large Jacobian matrix and needs reconstruction scheme for its calculation. The finite element (FE) model for the direct problem can be used to calculate J numerically. J is defined as:

$$J = \begin{vmatrix} \frac{\delta \ln I_1}{\delta D_1} & \frac{\delta \ln I_1}{\delta D_2} & \cdots & \frac{\delta \ln I_1}{\delta D_N} & \frac{\delta \ln I_1}{\delta \mu_{a1}} & \frac{\delta \ln I_1}{\delta \mu_{a2}} & \cdots & \frac{\delta \ln I_1}{\delta \mu_{aN}} \\ \frac{\delta \theta_1}{\delta D_1} & \frac{\delta \theta_1}{\delta D_2} & \cdots & \frac{\delta \theta_1}{\delta D_2} & \frac{\delta \theta_1}{\delta \mu_{a1}} & \frac{\delta \theta_1}{\delta \mu_{a2}} & \cdots & \frac{\delta \theta_1}{\delta \mu_{aN}} \\ \frac{\delta \ln I_2}{\delta D_1} & \frac{\delta \ln I_2}{\delta D_2} & \cdots & \frac{\delta \ln I_2}{\delta D_N} & \frac{\delta \ln I_2}{\delta \mu_{a1}} & \frac{\delta \ln I_2}{\delta \mu_{a2}} & \cdots & \frac{\delta \ln I_2}{\delta \mu_{aN}} \\ \frac{\delta \theta_2}{\delta D_1} & \frac{\delta \theta_2}{\delta D_2} & \cdots & \frac{\delta \theta_2}{\delta D_N} & \frac{\delta \theta_2}{\delta \mu_{a1}} & \frac{\delta \theta_2}{\delta \mu_{a2}} & \cdots & \frac{\delta \theta_2}{\delta \mu_{aN}} \\ \vdots & \vdots & \vdots & \vdots & \vdots & \vdots & \vdots & \vdots \\ \frac{\delta \ln I_M}{\delta D_1} & \frac{\delta \ln I_M}{\delta D_2} & \cdots & \frac{\delta \ln I_M}{\delta D_1} & \frac{\delta \ln I_M}{\delta \mu_{a1}} & \frac{\delta \ln I_M}{\delta \mu_{a2}} & \cdots & \frac{\delta \ln I_M}{\delta \mu_{aN}} \\ \frac{\delta \theta_M}{\delta D_1} & \frac{\delta \theta_M}{\delta D_2} & \cdots & \frac{\delta \theta_M}{\delta D_N} & \frac{\delta \theta_M}{\delta \mu_{a1}} & \frac{\delta \theta_M}{\delta \mu_{a2}} & \cdots & \frac{\delta \theta_M}{\delta \mu_{aN}} \end{vmatrix} \tag{2.3.3}$$

where M is the number of measurements and N is the number of nodes. b is the difference between the measurements and the calculation which is defined by:

$$b = \Phi^m - \Phi^c \tag{2.3.4}$$

Then the inverse problem is simplified as calculation of the root for $F(x) = \Psi'(x) = 0$. Two common methods have been used to get the root. One is gradient method, the iterative equation is:

$$x_{n+1} = x_n - \lambda_n F'(x_n) \tag{2.3.5}$$

Here λ_k is the step size to minimize the function $\lambda_k : \min_{\lambda>0} F(x_{n+1} - \lambda F'(x_n))$.

The other is Newton iteration method which can be expressed as:

$$x_{n+1} = x_n - \frac{F(x_n)}{F'(x_n)} \tag{2.3.6}$$

When the high order terms of the derivative are neglected, then we get:

$$F'(x) \approx 2J^T J \tag{2.3.7}$$

And hence $x_{n+1} = x_n + \left(J^T J\right)^{-1} J^T b$ (2.3.8)

The matrix $J^T J$ is typically a singular matrix and not invertible, LM method adds a factor λ to compromise between Gauss-Newton and the gradient method. The equation is as follows: [9]][15][16][17][21]

$$x_{n+1} - x_n = \left(J^T J + \lambda J\right)^{-1} J^T b \tag{2.3.9}$$

CHAPTER 3

INSTRUMENTATION

Generally, NIR-DOT systems can be divided into three different categories: time-domain (TD), frequency-domain (FD) and continuous wave (CW) systems. [17] In time-domain (CW) system, very short light pulses are injected into the tissue and transporting through it. Then the light pulses are attenuated and broadened in time, which can be measured with the appropriate detectors. In frequency-domain (FD) system, sinusoidal modulation of the source strength is typically from 100MHz to 1GHz which results in the propagation of photon-density waves inside the tissue. Phase shifts between the incident wave and the detected wave and the measuring amplitude differences exist in the acquired data. In continuous wave (CW) systems, light sources are constantly delivered into the tissue with the same amount of energy, and the time-independent intensities are measured by the detectors. For each of these optical imaging modalities, different types of hardware are required and different challenges on the image reconstruction process are faced. In this project, we used a novel technique called spread-spectral encoding method to achieve the light coupling and delivery, this technique is based on the CW mode.

3.1 The Design of Endoscopic NIR Probe

The endoscope near infrared optical tomography probe consists of 16 bare fibers. The diameter of each fiber is 600μm and the length of the fibers is 2m. One side of those 16 fibers was integrated into the tip of the endoscopic probe (made by black material to eliminate the light reflection) and all of them were circularly and evenly arranged. At the other side, the 16 fibers were separated as two branches: 8 of them (fiber number: 1, 3, 5, 7, 9, 11, 13, 15) were used as source-coupling fibers; the other 8 fibers (fiber number: 2, 4, 6, 8, 10, 12, 14, 16) were used as signal detector and light delivery channel.

At the probe tip, a 10mm diameter cone lens was used as a 90° circumferential light deflector. So the incident light could be deflected to the scanning plane of the endoscopic probe which perpendicular to the incident light itself. The 16 fibers and the cone-lens were mounted together by a 13mm diameter black sleeve, on the surface of which sixteen 1mm holes were drilled and sealed with transparent optical epoxy to serve as the aperture.

At the side of source-coupling fibers, a fiber bundle was made for the linear arrangement of 8 source fibers. The other branch was used as light signal detector and delivery channel which connected to the spectrometer and the CCD camera. Also the 8 signal detected fibers are linearly arranged.

The detailed sketch and the photos of the linear fiber bundle and the probe tip were shown in Figure 3.1

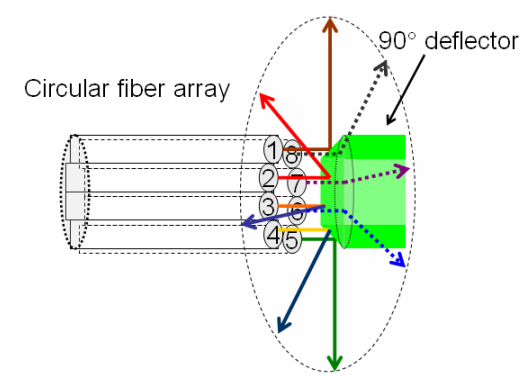

Figure 3-1 (a)

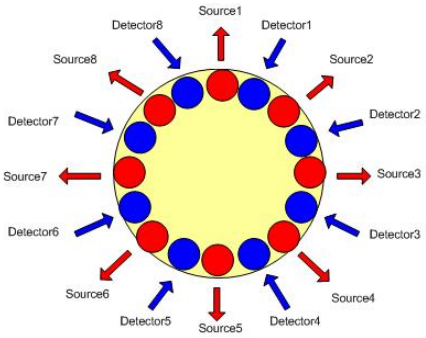

Figure 3-1 (b)

Figure 3-1 (c)

Figure 3-1 (d)

Figure 3.1. Sketches and Photo of Linear Fiber Bundle and Probe Tip

3.2 The Design of the Dual Wavelength Endoscopic Imaging System

The design of dual wavelength endoscopic NIR optical tomography imaging system was based on a novel approach of spread-spectral-encoding of a broadband light source in combination with linear-to-circular fiber bundling, by which multiple source/detector fibers could be enclosed in a probe for endoscopic NIR tomography.

This parallel sampling principle was similar to the previously published "spectral-encoding method based upon laser diodes (LDs)" by Dartmouth College. [18] However, due to the size limitation, it was infeasible to integrate the LD-based configuration into an endoscopic probe. Also, in the LD-based configuration, the

emission wavelength of each LD was controlled separately, which brought a lot of extra work and potential problems. To simplify this design, we used a broadband light source with spread-spectral-encoding technique, which preserved the feature of parallel sampling required for rapid imaging, and satisfied for the requirement of an endoscopic probe.

The key feature of the spread-spectral-encoding technique was to use broad band light source and diffraction grating to achieve multiple wavelengths detection. The diffraction grating was positioned at the focal plan of a collimating lens. After the dispersion of the grating, the dispersed light beam strips could be collimated by the lens and incident upon the linear fiber bundle of the endoscopic NIR probe which was located at the other focal plan of the lens. Since the 8 source fibers were linearly arranged, and the distance between each fiber was 600μm (to minimize the overlap of the light wavelength which collected by each fibers), the light wavelength which coupled to each fiber would be slightly different from each others. Then 8 light sources with different wavelength were spectrally encoded and parallel delivered to the tissue. Thus each fiber functions as a source and the NIR light can be parallelly delivered to the tissue. Then the light signals were collected by 8 detection fibers and delivered to a spectrometer. The spectrometer was used to spectrally decode the signals, allowing concurrent sampling of entire source-detector pairs by CCD camera.

To achieve dual wavelength detection, two broad-band light sources (wavelength centered at 780nm and 830nm, respectively) were used in this system. The two lights were delivered onto the diffraction grating. Because we wanted to make sure that two dispersed beam strips could be delivered exactly onto the same fiber bundle surface, the

disperse angle of two broadband lights must be equal to each other. However, the wavelengths of the two light sources were different. Based on the grating equation, the incident angles of these two light must have a certain difference.

$$m\lambda = d\left(\sin\alpha + \sin\beta\right) \tag{3.1}$$

where α is the incident angle of light source A, center wavelength of which is 780nm; β is the incident angle of light source B, center wavelength of which is 830nm; m is the diffraction order of the grating, which equals 1; And d is the grating period, here $d = 1/1200\,\text{mm}$.

Using equation 3.1, we calculated that the incident angle difference between two light sources was approximately equal to 5 degree. Due to the space limit, we put two reflection mirrors in front of the incident light beams, thus the incident beam could be reflected to the grating. Then we could easily control the incident angle (to the grating) difference by adjust the reflection angles of the two mirrors. The sketch and the test setup of this light incident design were shown in Figure 3.2.

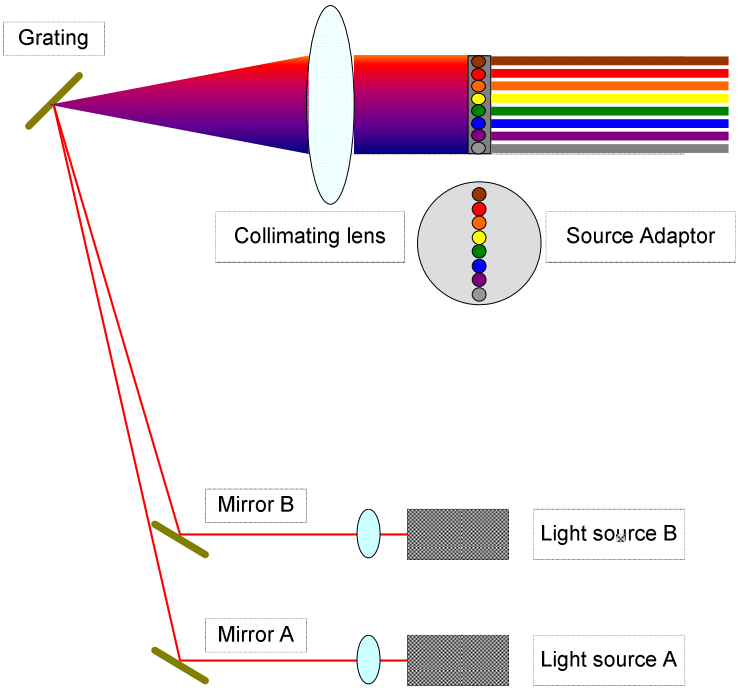

(a) Sketch of Dual-Band Light Delivery

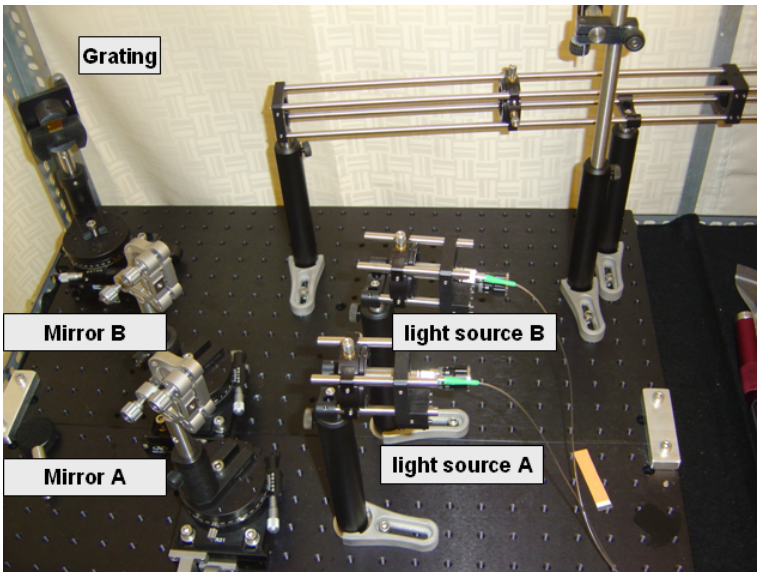

(b) Test Setup of Light Delivery Design

Figure 3.2. Sketch and the Test Setup of Light Incident Design

The dimension of the two beam strips at the fiber facet plane can be calculated as follows: [7]

$$L_{FWHM} = f \cdot \Delta\lambda_{FWHM} \Big/ \left[d\sqrt{1-(\lambda_0/d - \sin\alpha)^2} \right] \tag{3.2}$$

where f is the focal length of the planar-convex lens, $\Delta\lambda_{FWHM}$ is the source spectral bandwidth, λ_0 is the center wavelength, d is the grating period, and α is the beam incident angle with respect to the grating axis. For N bare fibers aligned side by side as shown in Figure 3.1(a), the spectral band coupled to the fiber bundle is:

$$\Delta\lambda_{bundle} = \Delta\lambda_{FWHM} \cdot N \cdot d_{fiber} \Big/ L_{FWHM} \tag{3.3}$$

Here d_{fiber} is the fiber diameter and N is the number of fibers.

In our imaging system, the grating period *p* was 1200 grooves/mm, the focal length f of the planar-convex lens was 300mm, and the fiber bundle was consisted of eight 600μm fibers. Due to CCD limitation, in order to acquire test data for both 780nm and 830nm bandwidth simultaneously, we have to use the 300 grove/mm grating in the spectrometer. The small grating period leads serious overlapping of the acquired light signal. To reduce the signals overlapping, we intentionally increased the intervals among the 8 source. So for the 780nm and 830nm broad band SLD NIR light source, 14nm bandwidth was coupled to the fiber bundle. Also we reduced the slit of the spectral-meter input. [4][20]

The overall sketch of the custom-made endoscopic dual-wavelength near-infrared optical tomography probe and the photograph of the completed instrument were shown in Figure 3.3.

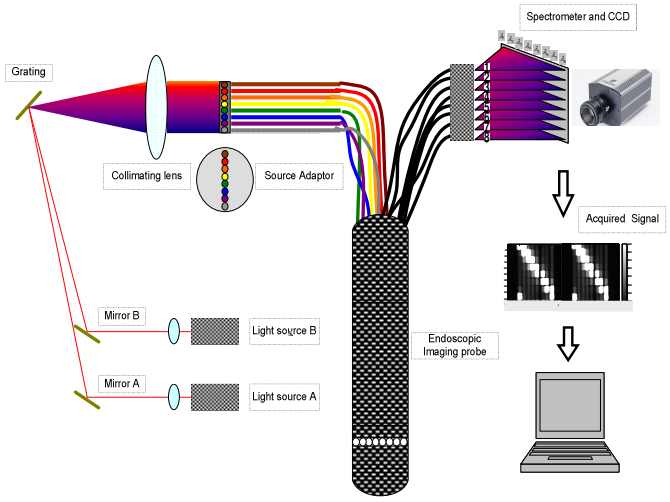

(a) Sketch of the Dual-Spectral NIR Imaging System

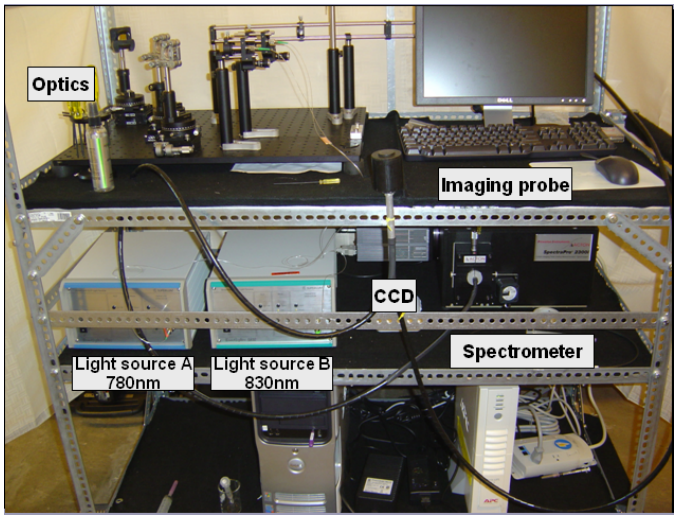

(b) Photo of the Dual-Spectral NIR Imaging System

Figure 3.3. Overall Sketch and the Photo of the Custom-Made Endoscopic Dual-Wavelength Near-Infrared Optical Tomography System

CHAPTER 4

CALIBRATION

Test data calibration is an essential step for the image reconstruction. First of all, for different tissue geometries, the boundary conditions need to be determined. Data calibration gives an initial estimation of the optical properties of the background for the image reconstruction. Second, the acquired test data contains many errors due to the non-uniformity among the different source-detector channels and the light intensity variation at the different test time. To eliminate those errors, it is necessary to do the test date calibration.

4.1 Calibration Principle

Beer-Lambert Law is a frequently used model-based method. The expression of the Beer-Lambert Law is given by:

$$\ln\left(\frac{I}{I_0}\right) = -l_p \mu_a + G \tag{4.1}$$

where I is the logarithm of the transmitted intensity, I_0 is the source output intensity, lp is the measurement of the optical pathlength. G is a constant factor related to the geometry of the tissue. In case of multiple source-detector pairs, the spatial derivative can be used to minimize the effect of G and determine the absorption

coefficient μ_a.

$$\frac{d\ln(I)}{d\rho} = -\frac{dl_p}{d\rho}\mu_a + \frac{dG}{d\rho} \tag{4.2}$$

Here ρ is the source-detector distance. If the geometrical factor *G* is not highly spatially dependent, then the term $\frac{dG}{d\rho}$ may produce a very small offset and can be neglected. Under the assumption, Equation (4.2) can be used to calculate the absorption coefficient μ_a. [22]

For scattering dominated medium, the analytic solution based on the diffusion equation (which simplified from the radiation transport theory) is more exact than the modified Beer-Lambert law. The diffusion equation can be solved analytically for simple geometries including the infinite and semi-infinite condition.

Assuming the tissue geometry is regularly shaped, the analytic solutions can be used with light measurement of phase and amplitude to calculate absorption and scattering coefficients.

For infinite medium condition, the analytic solution of the frequency-domain Green's function to the diffusion equation is listed below:

$$G_{Inf} = \frac{e^{-j\omega t}e^{-\alpha\rho}}{2(2\pi)^{\frac{3}{2}}\rho D} \tag{4.3}$$

Here, in order to estimate μ_a and μ_s, multiple source or detector locations can be used to approximate the spatial derivatives of the phase shift and intensity ratio which can be fit to their analytic counterpart.

$$\frac{d\phi}{d\rho} = \sqrt{\frac{\mu_a}{D}}\left[1+\left(\frac{\omega}{\mu_a c}\right)^2\right]^{1/4} \sin\left[\frac{\arctan\left(\frac{\omega}{\mu_a c}\right)}{2}\right] \tag{4.5}$$

$$\frac{d\left[\ln\left(\rho I_{ac}\right)\right]}{d\rho} = \sqrt{\frac{\mu_a}{D}}\left[1+\left(\frac{\omega}{\mu_a c}\right)^2\right]^{1/4} \cos\left[\frac{\arctan\left(\frac{\omega}{\mu_a c}\right)}{2}\right] \tag{4.6}$$

where I_{ac} is the photon density of the ac component, D is the diffusion coefficient defined as $\frac{1}{3\left(\mu_a + \mu_s'\right)}$, ρ is the source and detector distance. [22]

4.2 Test Data Calibration

In this study, the 8 source fibers were horizontally aligned (for horizontal spectral decoding) and the 8 detector fibers were vertically aligned (for vertical spatial separation). So the CCD acquired diffused signal is a two-dimensional light intensity map for all the 64 source detector pairs. Also, as mentioned in Chapter 3, the eight sources and eight detectors were evenly interlaced along the distal surface of the probe, so all the sources and detectors were symmetric with each others. Thus, for the total 64 sources-detector pairs, there were only four different source detector distances. Ideally, the 16 source-detector pairs which corresponding to same source detector distance should be identical to each other in homogenous medium. This feature could be used to calibrate the detected signal and compensate any non-uniformity among different source-detector channels.

The ideal raw data image is shown in Figure 4.1. The horizontal coordinate is eight

sources (from left to right, 1 to 8) and the vertical coordinate is eight detectors (from top to bottom,1 to 8), respectively.

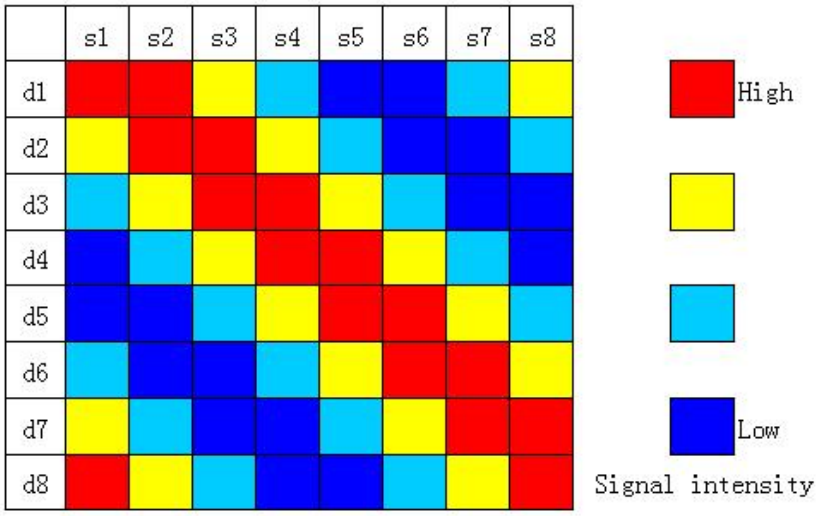

Figure 4.1. Ideal Raw Data Image

However, since the NIR light intensity profile is a Gaussian shape and we intentionally increased the intervals among the 8 source fibers to reduce the signals overlapping which caused by small grating period, the 16 source-detector pairs which corresponding to the same source detector distance were not identical any more. The source fibers which were placed in the center (source 4 and source 5) acquired much more energy than the source fibers which were placed at the two sides (source 1 and source 8). To mitigate this type of errors, we designed and fabricated a special light attenuator. Two elastic black chips were fixed together by a metal frame and a slit was remained between these two chips. Then a small screw was used to connect the metal and the top chip. The vertical position of this screw could be adjusted by tighten or release the screw. When we tighten this screw, the center part of the top chip was pushed down. So the center part of the slit between two chips was narrowed, but the two sides did not

changed. With this type of light attenuator, we can partially eliminate the errors which caused by the non-uniformity of the source signals.

The sketch and photo of this light attenuator were shown in Figure 4.2 (a) and (b). The CCD acquired raw data image with and without this attenuator were shown in Figure 4.3 (a) and (b)

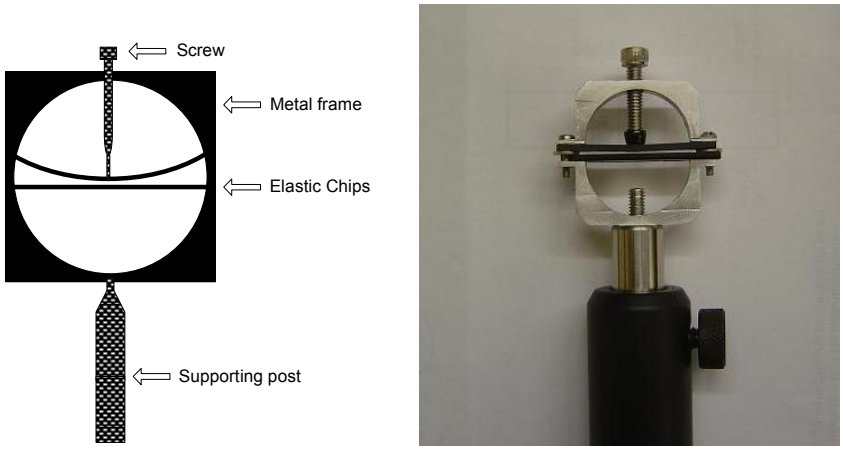

(a) The Sketch (b) Photo

Figure 4.2. Sketch and Photo of Light Attenuator

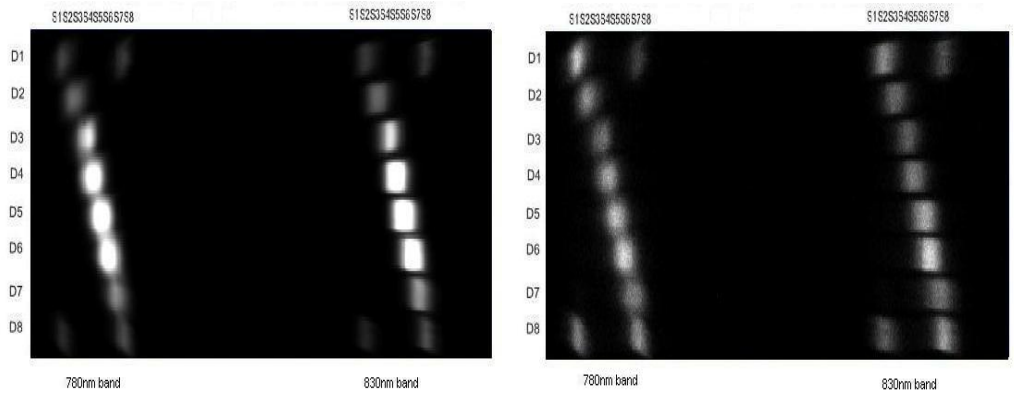

(a) Without Light Attenuator (b) With Light Attenuator

Figure 4.3. CCD Acquired Raw Data Image (with and without attenuator)

The source-detector array of the endoscopic NIR-DOT probe was placed at the boundary of the probe, and all the optical fibers were placed inside the probe. The

theoretical boundary condition can be treated as infinite boundary condition. Therefore, the relation between the received signal intensity and the source-detector distance is approximately defined by the following equation:

$$Ln(\rho I) = a \cdot \rho + b \tag{4.7}$$

where ρ is the distance between the each source-detector pair; I is the intensity of the signal detected; a and b are the linear fitting parameters that is defined by absorption coefficient μ_a and the scattering coefficient μ_s .[19][23]

The relationship between the source-detector distance and the signal intensity for homogeneous background and the heterogeneous data were shown in Figure 4.4(a), (b), (c) and (d). Before calibration, for all the source-detector distance, the signals intensity for both homogeneous background and heterogeneous data were quite different due to the system error and all kinds of noise. After calibration, both datasets for all the source-detector channels were uniform; also the signal responses for the symmetric channels were same with each other.

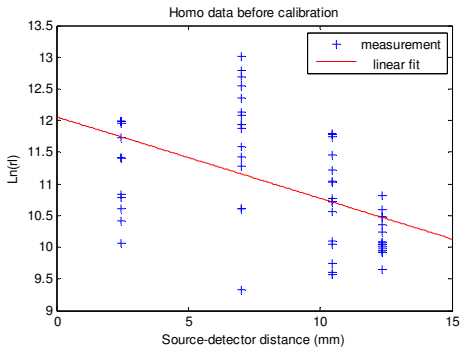

(a) Homo Data, before Calibration

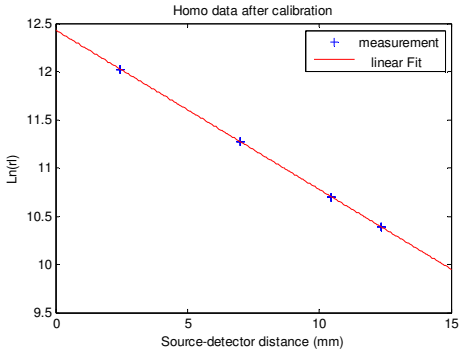

(b) Homo Data, after Calibration

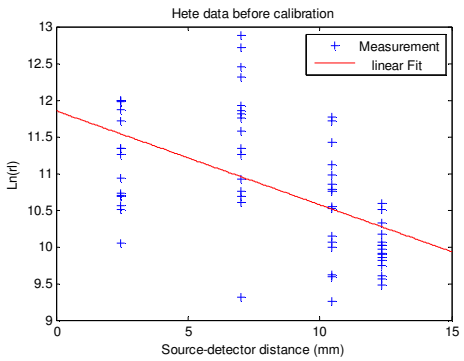

(c) Hete Data, before Calibration

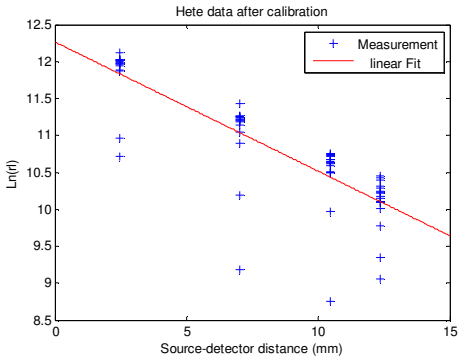

(d) Hete Data, after Calibration

Figure 4.4. Linear Data Fitting of both Homogeneous Background and Heterogeneous Data (before and after Calibration)

The signal intensity for non-calibrated and calibrated homogenous background/heterogeneous data along the 64 source-detector channels were shown in Figure 4.5 (a), (b), (c), (d). For the homogenous background, the non-calibrated data showed the different signal response for all the source-detector pairs; after calibration, the signal response was uniform for the pairs which have same source-detector distance. For the heterogeneous data, the shape of non-calibrated heterogeneous signal was changed due to the high absorbing object. After the calibration, the change of signal response which caused by the high absorbing object was kept. [24]

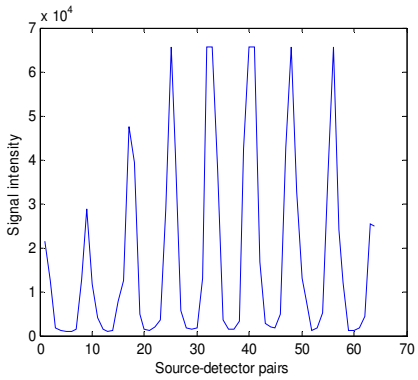

(a) Non-Calibrated Homo Data

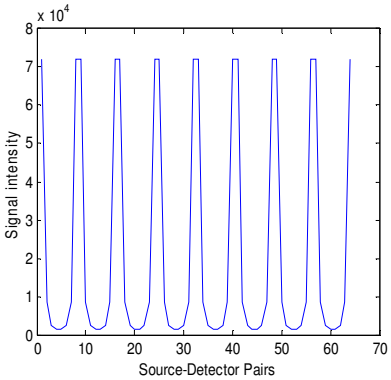

(b) Calibrated Homo Data

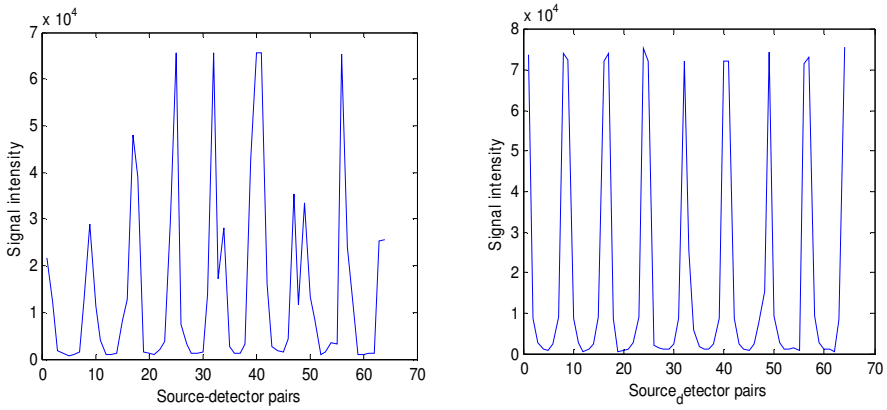

(c) Non-Calibrated Hete Signal (d) Calibrated Hete Signal

Figure 4.5. Homogeneous Background Data and Heterogeneous Data Calibration.

In this project, we used the software 'NIRFAST' which developed by Dartmouth Near-infrared group. This software is used by several groups for frequency domain optical data calibration and imaging reconstruction. NIRFAST calculates iteratively the offset between the homogenous data and the heterogeneous data. Then this offset is subtracted from the measured heterogeneous data.

The calibration procedures were:

1. Use the homogeneous phantom to acquire the background data and find out the 8×8 region of interest (ROI).

2. Calculate the analytical solution based on the model described by equations given above, and then compensate the eight source power to make them have uniform intensity.

3. Use the analytical model solution as the initial value; calculate the global absorption coefficient $\mu_{a(\mathrm{hom}o)}$ and scattering coefficient $\mu'_{s(\mathrm{hom}o)}$ by Finite Element Model (FEM).

4. Repeat step1~3 with heterogeneous phantom, calculate the heterogeneous

data $\mu_{a(hete)}$ and $\mu'_{s(hete)}$.

Then we can calibrate the heterogeneous data by:

$data_{calib(hete)} = data_{med(hete)} - \left(data_{med(\mathrm{hom}o)} - data_{calib(\mathrm{hom}o)}\right) - \left(data_{offset(hete)} - data_{offset(\mathrm{hom}o)}\right)$, Here $data_{offset(\mathrm{hom}o)}$ is an offset calculated between the measured homogenous data and the modeled homogenous data; $data_{offset(hete)}$ is another offset calculated between the measured heterogeneous data and the modeled heterogeneous data. The term $data_{offset(hete)} - data_{offset(\mathrm{hom}o)}$ can correct the system drift between the measurements of the homogenous phantom and the heterogeneous phantom.

CHAPTER 5

SYSTEM PERFORMANCE

5.1 Investigation of the True Value for the Heterogeneous Phantom Absorption Coefficient

In this Study, the diameter of the endoscopic NIR-DOT probe is quite small (out diameter is 13mm), so the distance between neighbored source-detector pairs was very short (approximately equals to 1mm) and the photons may not fully scattered. Under these circumstances, the reconstruction algorithm based on the diffusion theory may not fully correct. However, it still can be used for absorption coefficient μ_a reconstruction, and we need to use other methods to test the real value of μ_a, then compare the reconstructed $\mu_{a-recon}$ with the measured real $\mu_{a-measure}$ and find out the error of the NIR endoscopic probe. In this project, diluted India ink was used as the heterogeneous absorber to investigate the true value of absorption coefficient.

5.1.1 Mathematics Theory

In accordance with Beer-Lambert law, the attenuation coefficient of the diluted India ink is given by

$$\mu_t = -\frac{1}{t}\ln\left(\frac{I}{I_0}\right) \tag{5.1}$$

where I_0 is the light intensity of the water sample, I is the light intensity of the ink sample which held by the cuvette and t is the light path length. The attenuation coefficient of the ink sample μ_t is the sum of the absorption coefficient μ_a and the scattering coefficient μ_s.

$$\mu_t = \mu_a + \mu_s \tag{5.2}$$

And $$\mu_s = \frac{\mu_s'}{(1-g)} \tag{5.3}$$

where μ_s' is the reduced scattering coefficient, and g is called scattering anisotropy. It is the mean cosine value of the scattering angle and its typical value of biological tissue is 0.90~0.95.

In our study, a small curette which has 1mm path length was used to hold the diluted ink sample. Because the light path length of the curette was only 1mm, the India ink was a high absorption and low scattering coefficient material, and we used distilled water as media, the scattering coefficient μ_s of 1mm thickness ink-water mixture could be neglected. Then equation (5.2) can be simplified as follows:

$$\mu_t \approx \mu_a \tag{5.4}$$

Substitute equation (5.4) into (5.1) and subtract background intensity I_b from I_0 and I, we have

$$\mu_a = -\frac{1}{t}\ln\left(\frac{I - I_b}{I_0 - I_b}\right) \tag{5.5}$$

5.1.2 Test Setup

We built a system to measure the light intensity after the attenuation of the ink. This system is shown in Figure 5.1.

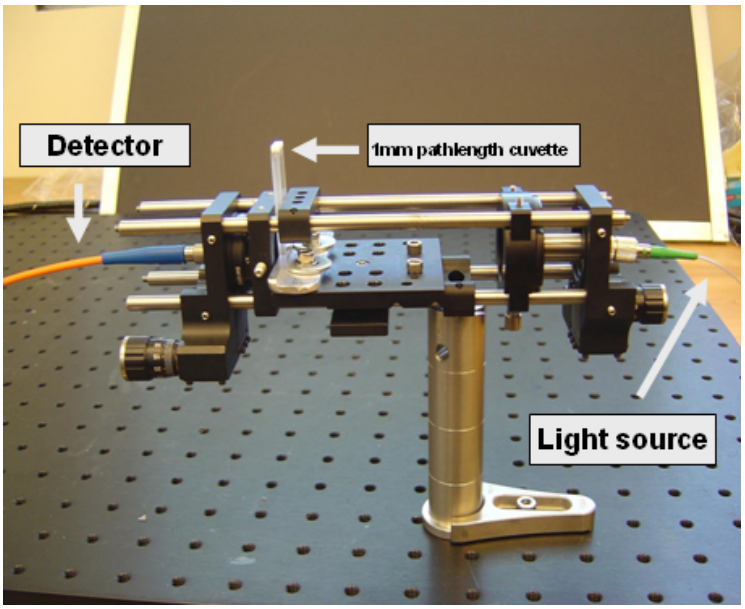

Figure 5.1. Test Setup for True Absorption Coefficient Investigation

Two SLD source ($\lambda = 780nm \quad and \quad 830nm$, respectively) were used as light source. The collimated near infrared light beam was delivered onto a cuevtte the position of which was fixed. The pathlength of the cuevtte was 1mm. Further, we placed two 1mm apertures over the incident light beam (not showed in Figure 5.1). The first one was placed in front of the cuevtte and the second one was placed behind the cuevtte. A fiber detector was placed behind the second 1mm aperture to collect the attenuated light. This design ensured only the perpendicular incident light could be collected by the detector. The detected light signals were delivered to the spectrometer and the CCD camera for further analysis. The whole system was placed in a black box to minimize the ambient light interference. [25]

5.1.3 Testing Procedure

First of all, we need to measure the background intensity I_b of the system. So we turn on the spectrometer and the CCD camera and get the 10 minutes average intensity without any signal input. This background intensity I_b should be subtracted from other measured value to acquire accurate test results.

Second, after the I_b was acquired, we injected distilled water into the cuvette and delivered the two light beams to the cuvette surface respectively to got the light intensity of a water sample I_{0-780} and I_{0-830}.

Then, 2ml distilled water was added into the small phantom cylinder which used as absorber holder in endoscopic NIR probe imaging reconstruction; then 1 drop (0.01ml) diluted ink with concentration=0.5% was added into the phantom cylinder and was fully mixed. Now the ink concentration in the phantom cylinder was increased from 0 to 0.00238%. Then the diluted ink sample (concentration=0.00238%) was injected into the cuvette and obtain the attenuated light intensity I_{780} and I_{830} respectively. After that, 99 drops diluted ink (concentration=0.5%) was gradually injected into the phantom cylinder, which resulted in the attenuated light intensity I_{780} and I_{830} for each concentration change. The ink concentration was increased from 0.00238% to 0.167%.

Repeat those steps 5 times and get the mean value of I_b, I_{0-780}, I_{0-830}, I_{780} and I_{830}.

5.1.4 Data Processing

For each wavelength, we obtained the mean value of the absorption coefficient for the diluted India ink (from 0 to 0.167%), which could be used to investigate the endoscopic NIR DOT system. The results for 780nm and 830nm NIR light were shown in Fig-2 (a) and (b) respectively.

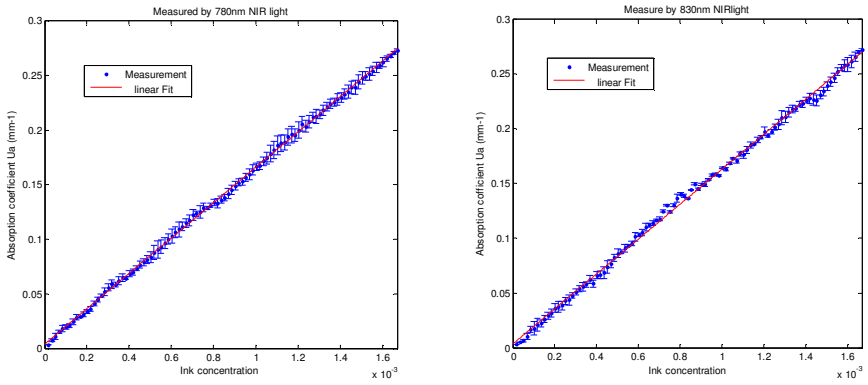

(a) Measured by 780nm NIR Light (b) Measured by 830nm NIR Light

Figure 5.2. Measured True Absorption Coefficient of Diluted India Ink (Concentration from 0 to 0.167%).

5.2 System Performance

To investigate the performance of the dual wavelength endoscopic NIR probe, we still used diluted India ink as the heterogeneous absorber. The probe was placed in the center of an intralipid tank which was made of black material. 1% Intralipid was poured in the tank to make an infinite uniform background.

Because both the 1% intralipid and the diluted India ink were liquid, we need to make a small cylindrical container with inner diameter of 10mm to hold the diluted ink. Here we used a custom made tissue like solid phantom (absorption coefficient=0.0056 mm−1 and scattering coefficient=1.03 mm−1) to fabricate the 10mm diameter cylindrical

container. The diffusion coefficient of this type of phantom is similar to the 1% intralipid. Also, to minimize the influence of the diffusion coefficient of the phantom, the wall of the cylindrical container was delicately fabricated and its thickness was less than 1mm. The total volume of this cylindrical container was 3 ml.

The phantom made cylindrical container was fixed nearby the surface of the probe by a supporting frame. To investigate the system uniformity for the absorption coefficient of the diluted ink, the frame was designed with 360 degree rotatable along the circumferential direction and length adjustable along the radius direction. So far the position of the cylindrical container relative to the probe was adjustable and the system uniformity could be measured.

The test system setup is illustrated in Figure 5.3 (a) and (b).

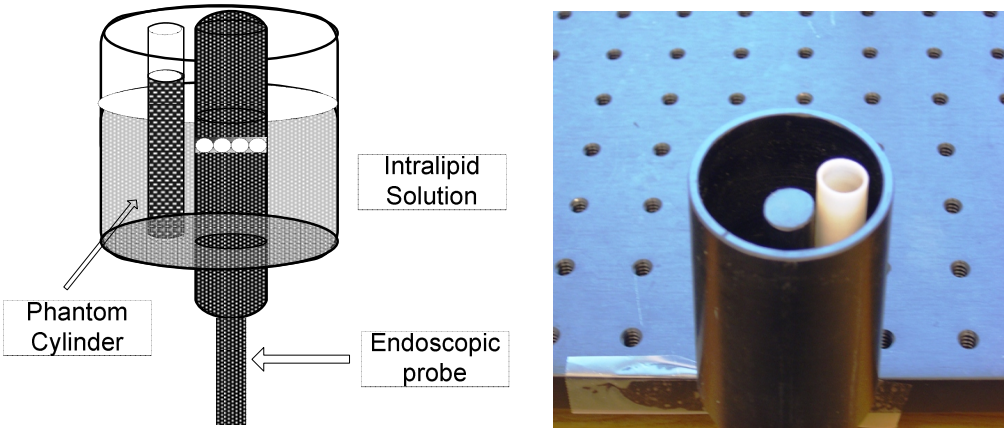

(a) Sketch (b) Photo

Figure 5.3. Sketch and Photo of India Ink Test System

5.3 Linearity of Absorption Coefficient Reconstruction

To evaluate the measurement linearity of the dual wavelengths endoscopic NIR probe, the measurement for the absorption coefficient variation was performed. The phantom made cylindrical container mentioned before was placed at the positions 7.5mm from the probe center to the outside surface of the cylindrical container along the radius direction. The intralipid tank was filled with 1% intralipid and 2 ml 1% intralipid was poured into the cylindrical container.

Then 1 drop (0.02ml) diluted ink with concentration=0.5% was added into the phantom cylindrical container and fully mix them. Now the ink concentration in the cylindrical container was increased from 0 to 0.0049%. After that, one frame picture for both 780nm and 830nm band was taken. Then 10 drops (0.02ml) diluted ink (concentration=0.5%) were gradually added into the cylindrical container and pictures were taken after every drops. The total India ink concentration in the cylindrical container was increased from 0% to 0.046% after 0.2ml (10 drops) 0.5% concentration India ink were added.

The comparison between the true absorption coefficient and the reconstructed absorption coefficients for both 780nm and 830nm band were shown in Figure 5.4 (a) and (b).

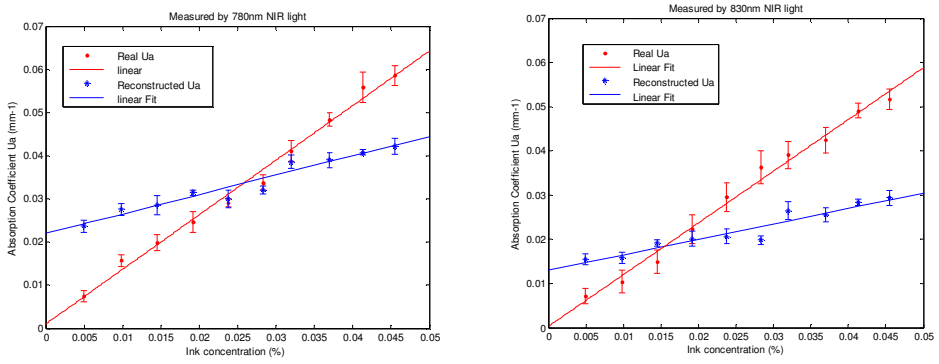

(a) Measured by 780nm Light Source (b) Measured by 830nm Light Source

Figure 5.4. True Absorption Coefficient and Reconstructed Absorption Coefficient. (Ink Concentration from 0~0.046%)

Figure 5.4 shows that for same concentration of the diluted India ink, the reconstructed value is different with the real absorption coefficient value; this is probably due to the reconstruction algorithm which based on the diffusion theory was not fully applicable for short source-detector distance. However, the reconstructed results for both two band lights showed good linearity and have similar trend like the measured value.

5.4 Uniformity of Absorption Coefficient Measurement

Uniformity of the absorption coefficient measurement was investigated along the radial and circumferential directions. The phantom made cylindrical container with diameters of 10mm was placed at the positions 7.5mm, 8.5mm and 10mm from the probe center to the outside surface of the cylindrical container along the radius direction. Figure 5.5 (a), (b), (c) provides an example of the reconstructed images for the phantom made cylindrical container filled with 0.167% concentration India ink. It indicates that the reconstructed image does not show very clear position change along the radius. This is probably due to the strong scattering medium; the resolution is not high enough to catch the small position change. However, the value of the absorption coefficient is decreased dramatically along with the increasing of the phantom-probe distance. Furthermore, when phantom-probe distance is greater than 11mm, the probe can not catch it anymore. The mean value and the standard deviation of the reconstructed absorption coefficients of diluted India ink with concentration equals to 0.167% for two wavelengths light sources

were listed in the Figure 5.6(a), (b).

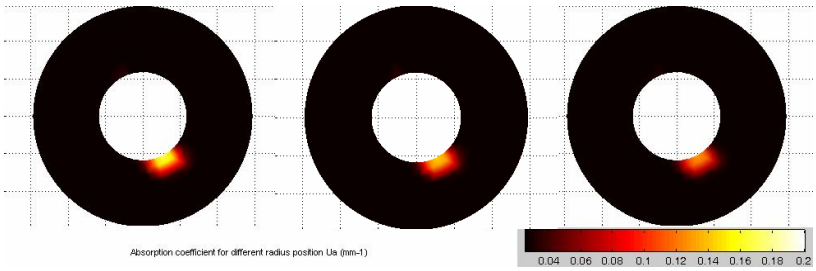

Figure 5.5. Reconstructed Absorption Coefficient Images; the Diluted India Ink was placed at Different Radius Position

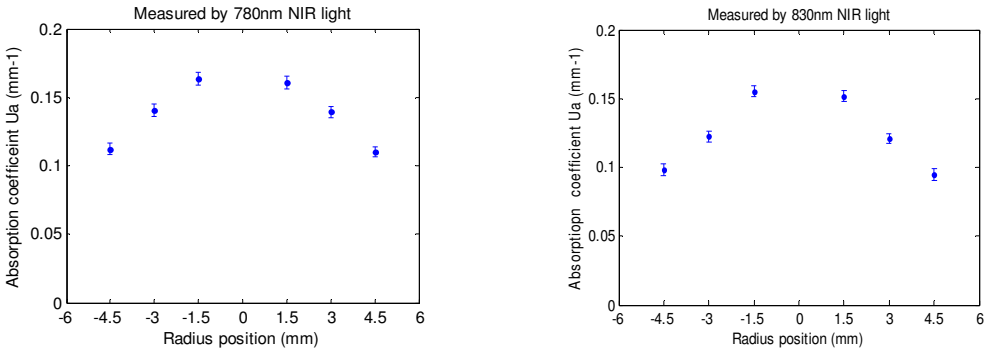

(a) Measured by 780nm NIR light (b) Measured by 830nm NIR light

Figure 5.6. Reconstructed Absorption Coefficients for Ink Sample at Different Radius Position

After the above measurement was finished, the cylindrical container was placed aside 16 source/detector locations interspersed every 22.5° to evaluate the measurement uniformity of the absorption coefficient along the circumferential direction. Also the diluted India ink concentration was 0.167%. The reconstructed images were shown in Figure 5.7. The comparison between the true absorption coefficients and the reconstructed absorption coefficients for 780nm and 830nm band reconstructed absorption coefficients at all 16 locations were shown in Figure 5.8.

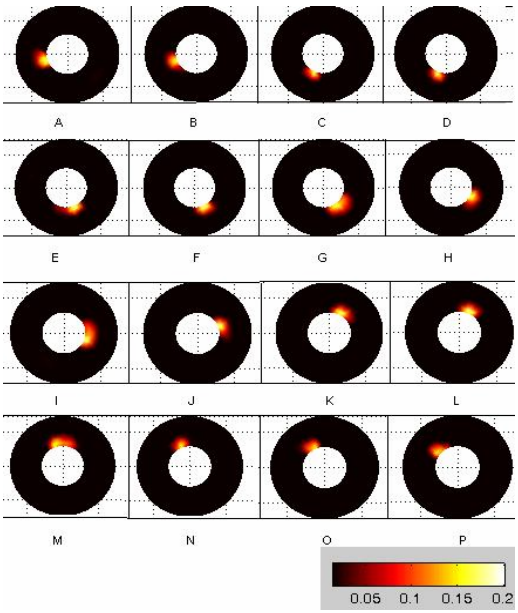

(a) Absorption Coefficient for 16 Positions (from 22.5 to 360 Degree), Measured By 780nm NIR Light

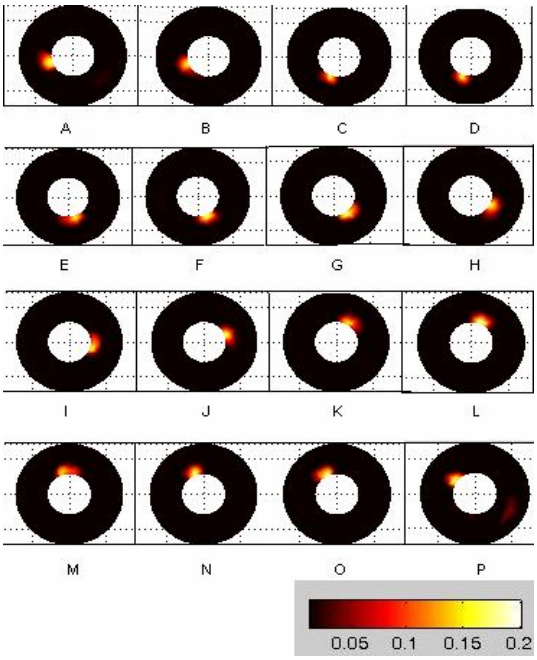

(b) Absorption Coefficient for 16 Positions (from 22.5 to 360 Degree), Measured By 830nm NIR Light

Figure 5.7. Reconstructed Images for Different Circumferential Location

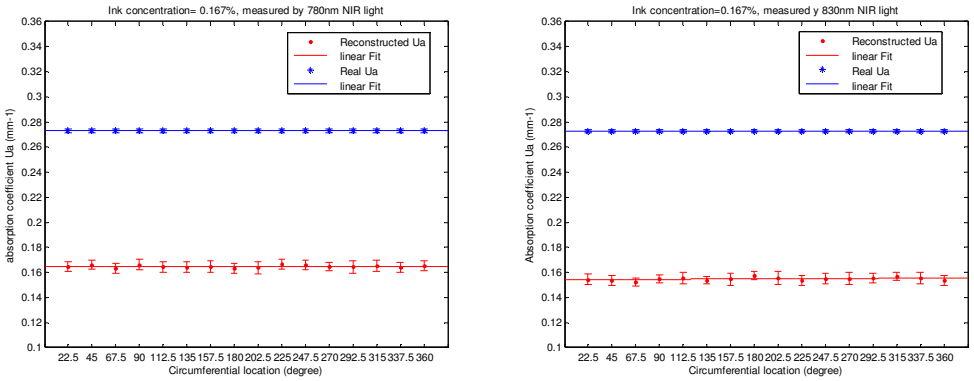

(a) Measured by 780nm NIR light (b) measured by 830nm NIR light

Figure 5.8. True Absorption Coefficient and Reconstructed Absorption Coefficients for 780nm and 830nm Band at all 16 Circumferential Locations. (Ink Concentration is 0.167%)

5.5 Imaging Multiple Objects

The capability of imaging multiple objects is qualitatively demonstrated in Figure 5.9, where one, two, three absorbers were immersed successively into the intralipid solution. Objects at multiple locations could be clearly identified, while the presence of more objects has the overall effect of lowering the recovered absorption of each of the other objects. This is a well-known feature of diffuse imaging. The ability to recover multiple objects helps to confirm that the system will perform well in more complex tissues such as small animal studies.

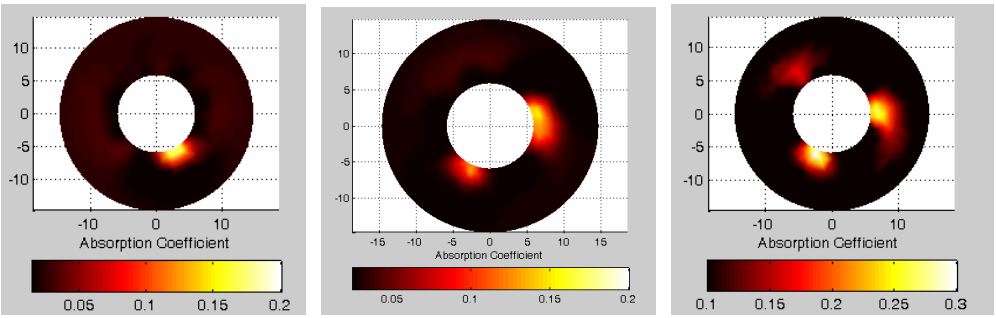

(a) One Absorber (b) Two absorber (c) Three Absorber

Figure 5.9. Capability of Imaging Multiple Objects. 1~3 Objects were placed into Intralipid Solution and Imaged, from left to right.

CHAPTER 6

BLOOD INVESTIGATION

Scientists have found that the tumor has different hemoglobin concentration respected to the normal tissue. In general, the total hemoglobin concentration in cancer tissue is higher than the normal tissue due to the high degree of vascularity.

The absorption coefficient of the human tissue is related to the concentration of the main chromophors which exist in human body such as the oxy-hemoglobin (HbO), deoxy-hemoglobin (Hb) and water. As mentioned before, in near-infrared window (600nm~900nm), compared to the hemoglobin, the absorption by the water can be neglected, so NIR-DOT has been used for cancer detection because the higher hemoglobin concentration can provider high contrast imaging for internal organ. [26]

From Figure 6.1, we can find that the oxygenated hemoglobin and deoxygenated hemoglobin have different variations of absorption according to the near-infrared wave-length. For oxy-hemoglobin, the absorption coefficient gradually increases along with the light wavelength increasing; for deoxy-hemoglobin, it has opposite trend. At 780nm band, the absorption coefficient of deoxy-hemoglobin is higher than the oxygenated one, but in the 830nm band, the oxy-hemoglobin has higher absorption coefficient. So we can use those two wavelength NIR lights to quantify the total hemoglobin concentration (HbT) and the oxygen saturation (StO2) changes of the blood.

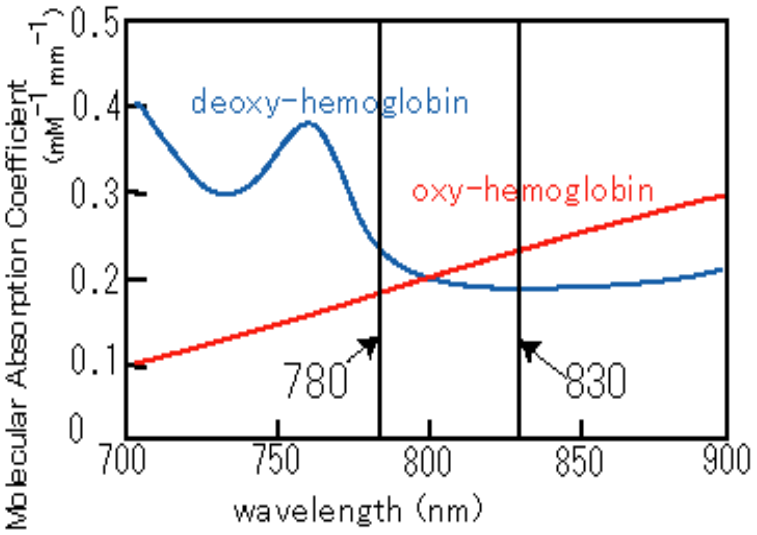

Figure 6.1. Different Variation Trends for Oxy-Hemoglobin and Deoxy-Hemoglobin at 780nm and 830nm NIE Band.

In this chapter, the test for the hemoglobin concentration and the oxygen saturation changes are depicted and the preliminary results are presented.

6.1 Calculation for the HbT and StO2 Test

The absorption coefficient μ_a^{λ} of HbO is related to the near infrared wavelength λ. It can be calculated by equation (6.1).

$$\mu_a^{\lambda} = \varepsilon_{HbO}^{\lambda}[HbO] + \varepsilon_{Hb}^{\lambda}[Hb] \tag{6.1}$$

Where $\varepsilon_{HbO}^{\lambda}$ and $\varepsilon_{Hb}^{\lambda}$ are the extinction coefficient of the tissue when the wavelength is λ. If we deliver two NIR light with different wavelength (λ_1 and λ_2) into human tissue, then the concentration of the $[HbO]$ and $[Hb]$ can be calculated by following equations: [27]

$$[HbO] = \frac{\mu_a^{\lambda_1}\varepsilon_{Hb}^{\lambda_2} - \mu_a^{\lambda_2}\varepsilon_{Hb}^{\lambda_1}}{\varepsilon_{HbO}^{\lambda_1}\varepsilon_{Hb}^{\lambda_2} - \varepsilon_{HbO}^{\lambda_2}\varepsilon_{Hb}^{\lambda_1}} \tag{6.2}$$

$$[Hb] = \frac{\mu_a^{\lambda_2}\varepsilon_{HbO}^{\lambda_1} - \mu_a^{\lambda_1}\varepsilon_{HbO}^{\lambda_2}}{\varepsilon_{HbO}^{\lambda_1}\varepsilon_{Hb}^{\lambda_2} - \varepsilon_{HbO}^{\lambda_2}\varepsilon_{Hb}^{\lambda_1}} \tag{6.3}$$

Here $\varepsilon_{HbO}^{\lambda_1}$ and $\varepsilon_{Hb}^{\lambda_1}$ are the extinction coefficients of the oxygenated hemoglobin (HbO) and deoxygenated hemoglobin (Hb) when the wavelength is λ_1; $\varepsilon_{HbO}^{\lambda_2}$ and $\varepsilon_{Hb}^{\lambda_2}$ are the extinction coefficients of the HbO and Hb when the wavelength is λ_2; In this project, we select the $\lambda_1 = 780nm$ and $\lambda_1 = 830nm$, and the value of $\varepsilon_{HbO}^{\lambda_1} = 71$, $\varepsilon_{Hb}^{\lambda_1} = 107.544$, $\varepsilon_{HbO}^{\lambda_2} = 97.4$ and $\varepsilon_{Hb}^{\lambda_2} = 69.304$ comes from the Oregon Medical Laser Center (http://omlc.ogi.edu), and the unit is $(mm^{-1})/(moles/liter)$.

Then we can obtain the total hemoglobin concentration and the blood oxygen saturation StO2 by: [28][29][30]

$$[HbT] = [HbO] + [Hb] \tag{6.4}$$

$$[StO2] = \frac{[HbO]}{[HbT]} \times 100\% \tag{6.5}$$

6.2 Instrumentation Design for Blood Test

In this project, 500ml fresh sheep blood was used to investigate the HbT and StO2 changes. In order to monitor the continuous change; we designed a blood circulation system to oxygenate the blood continuously and took the imaging of the oxygenated blood for both two NIR light band simultaneously. In the system, a small pump, three soft tygon tubing, a small cylinder made of phantom and one blood tank were used.

The blood tank was used to hold the blood, 5 holes were drilled on its cover. The

small pump was used to generate the circulation. A soft tygon tubing is used to connect the pump and the blood tank: one side was inserted into the blood tank; the other side was connected to the liquid input of the pump. The 10mm diameter small cylinder which was made by solid phantom was used as imaging object. At the top and the bottom of this small cylinder, we drill a 6.35mm (1/4 inch) hole. The other two soft tygon tubings (1/4 inch od) were inserted into those two holes and sealed with epoxy. Now the two tubing and the small cylinder were connected together as a blood channel. Then one side of this channel was connected with the output of the pump; the other side was inserted into the blood tank for the entire blood circulation. [31][32]

In order to make the blood fully oxygenated and de-oxygenated， we used two hard plastic tubing to deliver Oxygen and Nitrogen into the blood.

The overall sketch and photo of this blood circulation channel are shown in Figure 6.2 (a) and (b).

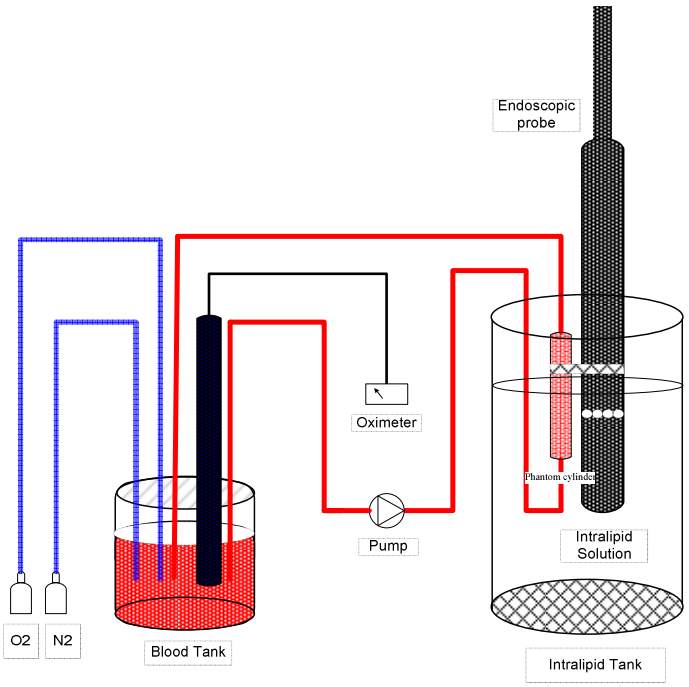

(a) Sketch of the Blood Oxygenation and Circulation System

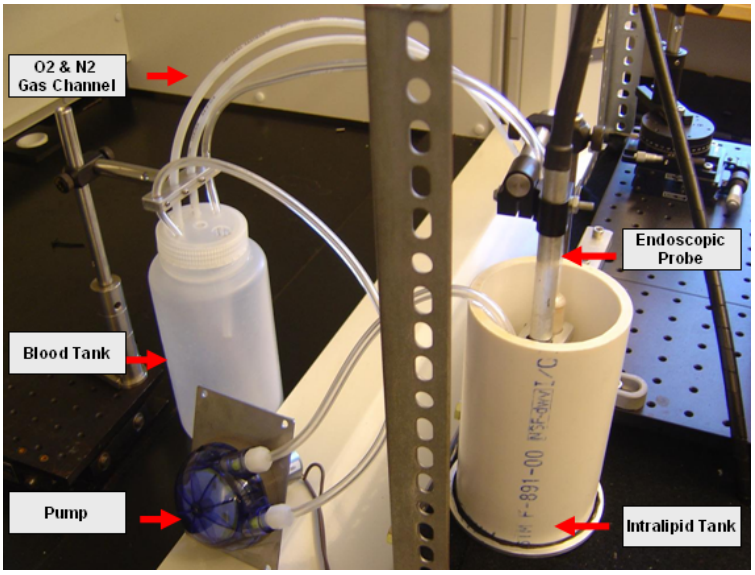

(b) Photo of Test Setup

Figure 6.2. Sketch and Photo of Blood Test Setup

6.3 Test Procedure and Result

To evaluate the HbT and StO2 of the sheep blood, the measurement for the hemoglobin absorption coefficient variation was performed.

During the blood HbT and the StO2 test, the blood holder was fixed in the ventilation hood. 300 ml sheep blood was placed in the blood tank. Here two hard plastic tubing were used to deliver the Oxygen and Nitrogen into the blood. For the blood circulation channel mentioned above, the cylinder part was fixed nearby the NIR-DOT probe at the 7.5mm positions (from the probe center to the outside surface of the cylindrical container, along the radius direction) and both sides of this channel were also inserted into the blood tank. We placed an oxi-meter into the blood to monitor the blood oxygen saturation level. Then the probe and the phantom cylinder were immerged into an intralipid tank which filled with 1% intralipid.

We took one image of pure intralipid medium as uniform background, then continuously delivered Nitrogen into the blood tank and used the oxi-meter to monitor the StO2 of the blood. After the readout of the oxi-meter showed stable (in general is around 8% but not 0%), we started the pump. The blood was continuously pumped into the circulation channel through the soft tygon tubing, after the connected cylinder was filled, it would go back to the blood tank. Now we took one frame picture for both 780nm and 830nm bands NIR light simultaneously as the heterogeneous data.

Then we gradually increased the gas flow of the Oxygen and used the oxi-meter to monitor the increased blood StO2 level. For each different StO2 level, we adjusted the two gas flows to maintain the StO2 value at this level, and then took one dataset. Test would be stopped until the readout of the oxi-meter become stable. Due to the precision

of the gas regulator, there was always some fluctuation, especially for lower StO2 level; so we could not acquire stable low level StO2. Also, due to the temperature control, leakage of gas from the blood tank, and we could not make the O2 fully dissolved in the blood, so the blood could not be fully oxygenated. However, the increasing trend of the blood StO2 level was recorded.

The test results for changed absorption coefficient are illustrated in Figure 6.3.

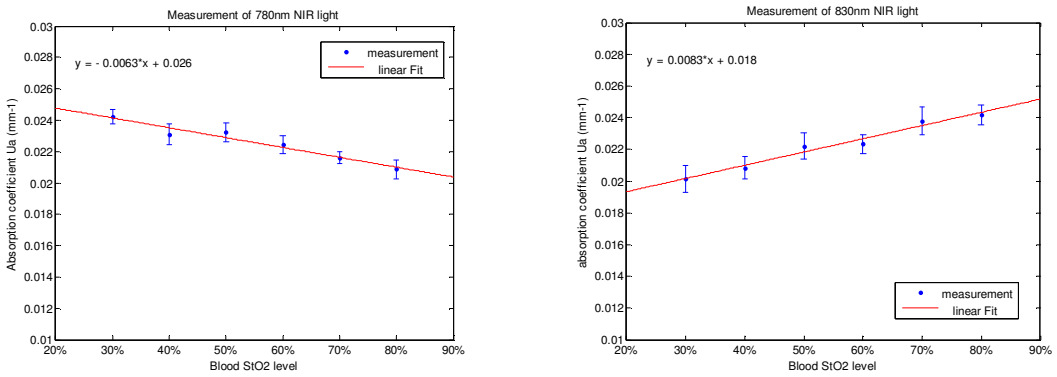

(a) Measurement of 780nm NIR light (b) Measurement of 830nm NIR light

Figure 6.3. Variation of the Hemoglobin Absorption Coefficient along with the StO2 Changes

The reconstructed total hemoglobin concentration (HbT) and the changed StO2 level were illustrated in Figure 6.4 (a), (b) and Figure 6.5 (a), (b). In our test setup, although the oxygen saturation level changed by input O2 or N2 gas into the blood tank, the total hemoglobin concentration did not change. From Figure 6.4 and Figure 6.5, one can find that the reconstructed HbT value also remained relatively stable; and the reconstructed StO2 value shows increasing trend along with the Oximeter readout.

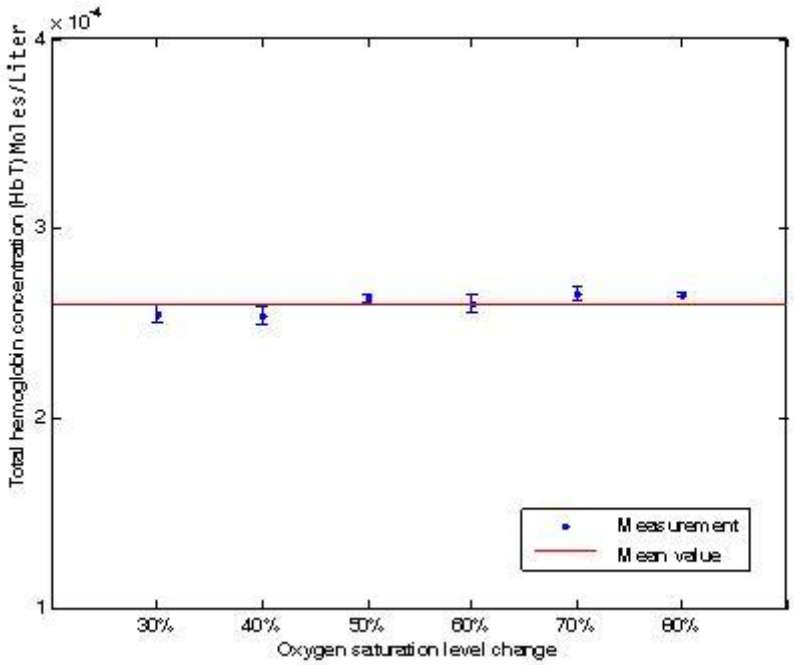

(a) Reconstructed Total Hemoglobin Concentration (HbT) Level along with the Oxygen Saturation Level Change

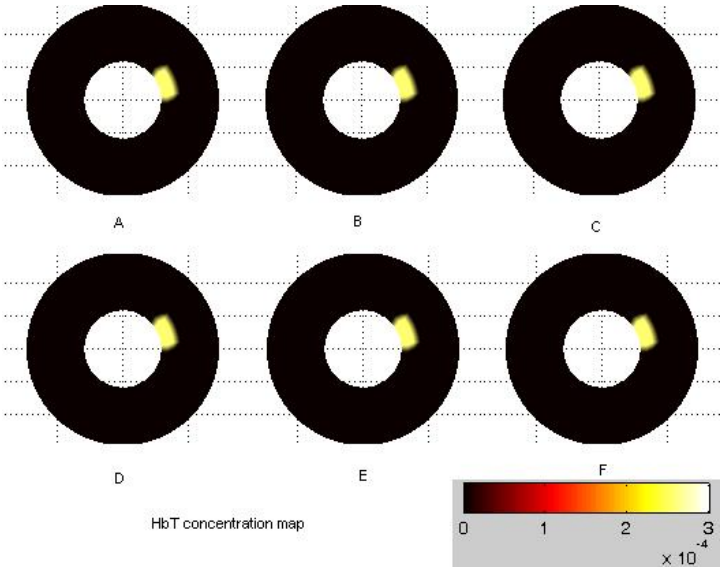

(b) Reconstructed Total Hemoglobin Concentration (HbT) Map

Figure 6.4. Reconstructed Total Hemoglobin Concentration (HbT)

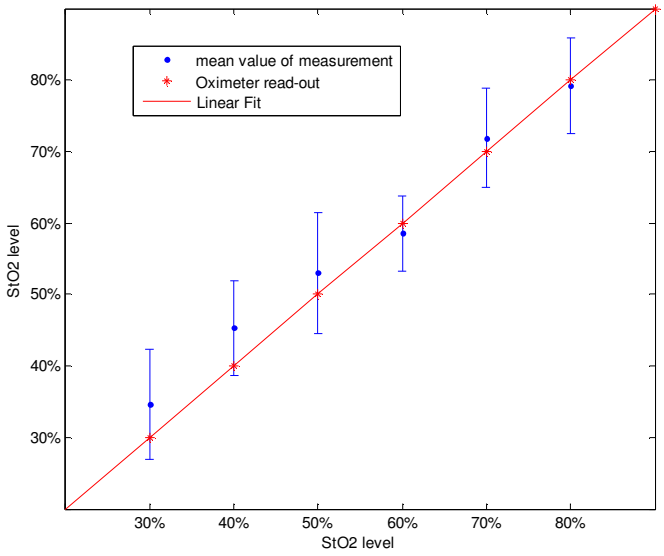

(a) Reconstructed StO2 Level Changes

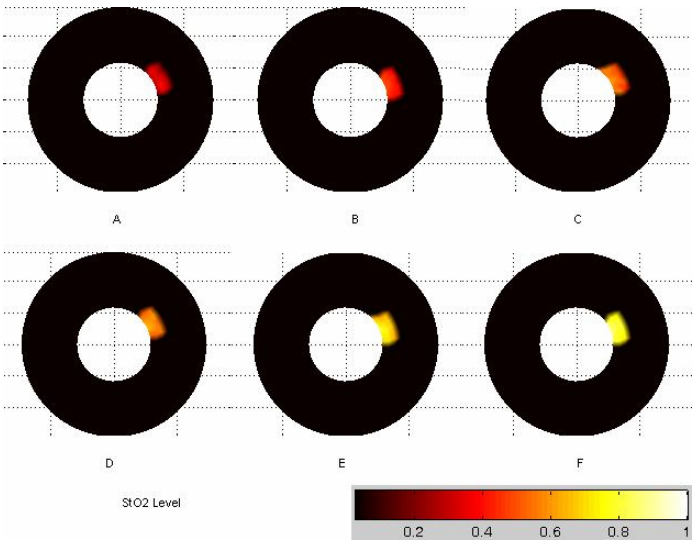

(b) Reconstructed StO2 Level Images

Figure 6.5. Reconstructed StO2 Value Changes and the StO2 Image

CHAPTER 7

CONCLUSION

7.1 Dual-Spectral Endoscopic NIR-DOT

Cancer detection and early diagnosis with optical imaging is not a novel idea. However, considerable progress has been made toward this biomedical imaging modality that uses near-infrared light to image biomedical tissue only since15 years ago. Despite its low resolution, NIR optical tomography acts as an important role in tumor research; detection today depends on its unique ability to assess functional and molecular cancer characteristics. Also the NIR-DOT is compatible with most other imaging techniques that allow the creation of combined modalities, which means it can be combined with other type imaging approach which has higher resolution and provide more accurate detection.

For the human tissue, the light absorption in the NIR window is mainly caused by oxy-hemoglobin and deo-hemoglobin. The different optical diffusion coefficients for both oxygenated and deoxygenated hemoglobin in the near infrared band allow the total hemoglobin concentration (HbT) and the oxygen saturation of the blood (StO2) can be quantitatively measured by implementing dual-spectral near-infrared diffuse optical tomography. This natural characteristic renders NIR diffuse optical tomography to be developed into a unique noninvasive technology for tissue imaging and quantitative vascularity analysis. Because it is relatively economical and can acquire data

continuously, NIR-DOT may be used for real-time monitoring.

In this project, the phantom study and the blood test were performed; the preliminary results showed that the endoscopic NIR-DOT probe could reveal the absorption coefficient changes of the heterogeneous objects and the blood StO2 level changes by implementing dual-spectral detection.

7.2 Future Works

However, the reconstruction accuracy of the endoscopic NIR-DOT probe needs to be improved further due to the following reasons:

7.2.1 Develop Reconstruction Algorithm for Small Scale Probe

The diffusion theory is only applicable in cases where $\mu_s' >> \mu_a$ and the smallest source-detector distance is $>> 1/\mu_s'$. In this project, to make the probe suitable for trans-rectal detection, the out diameter of the probe was only 13mm and hence the smallest source-detector distance was only around 2mm. Thus the probe only meets the first requirement. Under this condition, the reconstruction algorithm based on the diffusion equation may not be fully applicable for this small size probe and will lead to errors in the reconstructed result.

Further, the change of the hemoglobin concentration and the oxygen saturation along with the heart beating is very useful for cancer detection. To image this type of change, the imaging speed needs to be improved, which means more light energy needs to be coupled to the endoscopic probe. Because the smaller the probe diameter, the more light energy can be concentrated to the imaging area, based on the structure

of the current probe, we designed and fabricated a smaller endoscopic imaging probe with only 5mm out diameter. The smallest source-detector distance of the 5mm probe was less than 1mm. This smaller source-detector distance also faced reconstruction algorithm problem and needs to be resolved.

7.2.2 Broad Band Light Source Compensation

In the project, we used the broad band laser as light source; the coupled bandwidth for each source was 14 nm. From the Figure 6.1, one can find that from the 770nm to 790nm band, the absorption coefficient of the deoxy-hemoglobin has very high change ratio. This means for the 780nm band NIR light souce, the 8 source fibers have different measurements, which bring certain errors into the heterogeneous data and need to compensate it in order the eliminate this type of error.

Here we hypothesize that an iterative method can possibly be used to correct the un-uniform measurement of the broadband light source. First of all, we can use the analytical model solution as the initial guess value to calculate the global absorption coefficient $\mu_{a(initial)}$ by Finite Element Model (FEM). Substitute $\mu_{a(initial)}$ into forward model and get the $data_{(f0)}$. Then we can use inverse model to reconstruct the test acquired heterogeneous data $data_{(test)}$ and obtain the $\mu_{a(test)}$, substitute $\mu_{a(test)}$ into forward model and get the $data_{(f1)}$ .Due to the difference between $\mu_{a(test)}$ and $\mu_{a(initial)}$, $data_{(f0)}$ and $data_{(f1)}$ must be different, so we can get $\Delta_{data(1)} = data_{(f1)} - data_{(f0)}$.

Secondly, $\Delta_{data(1)}$ can be used to correct the test acquired data $data_{(test)}$.

Subtracting $\Delta_{data(1)}$ from $data_{(test)}$, we can get $data_{test-\Delta_{data(1)}}$. Then we can substitute it into inverse model and get $\mu_{a(test-\Delta 1)}$, after that forward model can be used to get $data_{(f2)}$. Now we can get $\Delta_{data(2)} = data_{(f2)} - data_{(f1)}$.

Similarly, the $data_{test-\Delta_{data1}}$ can be corrected with $\Delta_{data(2)}$. When $\Delta_{data(2)}$ is subtracted from $data_{test-\Delta_{data(1)}}$, we can get $data_{test-\Delta_{data(1)}-\Delta_{data(2)}}$. Substitute it into inverse model and get $\mu_{a(test-\Delta 1-\Delta 2)}$ and use forward model get $data_{(f3)}$. Now we can get $\Delta_{data(3)} = data_{(f3)} - data_{(f2)}$ and hence the corrected heterogeneous data $data_{test-\Delta_{data(1)}-\Delta_{data(2)}-\Delta_{data(3)}}$. When the $\Delta_{data(n)}$ can be neglected compare with $data_{test-\Delta_{data1}-.....-\Delta_{data(n-1)}}$, the iteration can be stopped.

We expect that this type of iteration can minimize the error caused by absorption coefficient variation, because at the initial guess, the diffusion coefficient was supposed to be uniform for different NIR light wavelengths. However, using narrow band light source (such as 4nm bandwidth) will improve the reconstruction accuracy.

REFERENCES

[1] Axel Glaessgen, '*Markers of Differentiation and Prognosis in Prostate Cancer – A Morphological and Immunohistochemical Study*', Thesis for doctoral (Ph.D) of Science, 2008.

[2] Subhadra Srinivasan, Brian W. Pogue, Shudong Jiang, Hamid Dehghani, Keith D. Paulsen, "*Spectrally Constrained NIR tomography for Breast Imaging: Simulations and Clinical Results*", Thayer School of Engineering, Dartmouth College, Hanover NH 03755

[3] Brian W. Pogue, Shudong Jiang, Hamid Dehghani, Christine Kogel, Sandra Soho, Subhadra Srinivasan, Xiaomei Song, Tor D. Tosteson, Steven P. Poplack, Keith D. Paulsen, "*Characterization of hemoglobin, water, and NIR scattering in breast tissue: analysis of intersubject variability and menstrual cycle changes*", Journal of Biomedical Optics, May/June 2004, Vol. 9 No. 3

[4] Daqing Piao, Shudong Jiang, Subhadra Srinivasan, Hamid Dehghani, and Brian W. Pogue, "*Video-rate near-infrared optical tomography using spectrally encoded parallel light delivery*", Optics Letters / Vol. 30, No. 19 / October 1, 2005

[5] Daqing Piao, Hao Xie, Weili Zhang, and Jerzy S. Krasinski, '*Endoscopic, rapid near-infrared optical tomography*', Optics Letters, Vol. 31, No. 19, October, 2006.

[6] Andrew K. Dunn, Anna Devor, Hayrunnisa Bolay, Mark L. Andermann, Michael A. Moskowitz, Anders M.Dale and David A. Boas, '*Simultaneous imaging of total cerebral hemoglobin concentration, oxygenation, and blood flow during functional activation*', Optics Letters / Vol. 28, No. 1 / January 1, 2003

[7] Daqing Piao, Brian W. Pogue, '*Rapid near-infrared diffuse tomography for hemogynamic imaging using a low-coherence wideband light source*', Journal of Biomedical Optics, 12(1), 014016, Jan 2007.

[8] S R Arridge, '*Optical tomography in medical imaging*', Inverse Problems, 15 (1999) R41-R93.

[9] S R Arridge, M Cope and D T Delpy, '*The theoretical basis for the determination of optical pathlengths in tissue: temporal and frequency analysis*', Phys. Med. Boil., 1992, Vol.37, No.7, 1531-1560.

[10] Brian W Pogue and Michael S Patterson, '*frequency-domain optical absorption spectroscopy of finite tissue volumes using diffusion theory*', Phys. Med. Biol. 39 (1994) 1157-1180.

[11] Kui Ren Gassan S. Abdoulaev, Guillaume Bal, Andreas H. Hielscher, '*Algorithm for solving the equation of radiative transfer in the frequency domain*', Optics Letters, Vol. 29, No.6, March, 2004.

[12] Wooseok Ko, Yoonkeun Kwak and Soohyun Kim, '*Measurement of optical coefficients of tissue-like solutions using a combination methods of infinite and semi-infinite geometries with continuous near infrared light*', Japanese Journal of Applied Physics, Vol. 45, No 9A 2006, pp. 7458-7462

[13] Arnold D. Kim, '*Transport theory for light propagation in biological tissue*', J.Opt. Soc. Am. A/ Vol.

21, No. 5, May 2004.

[14] Alexander D. Klose, Uwe Netz, Jurgen Beuthan, Andreas H. Hielscher, '*Optical tomography using the time-independent equation of radiative transfer-Part 1: forward model*', Journal of Quantitative Spectroscopy & Radiative Transfer 72 (2002) 691-713.

[15] Alper Corlu, Regine Choe, Turgut Durduran, Kijoon Lee, Martin Schweiger, Simon R. Arridge, Elizabeth M. C. Hillman, and Arjun G. Yodh, '*Diffuse optical tomography with spectral constraints and wavelength optimization*', Applied optics, Vol.44, No.11, 10 April 2005.

[16] Alexander D. Klose, Andreas H. Hielscher, ' *Optical tomography using the time-independent equation of radiative transfer-Part 2: inverse model*', Journal of Quantitative Spectroscopy & Radiative Transfer 72 (2002) 715-732

[17] Alexander D Klose and Andreas H Hielscher, '*Quasi-Newton methods in optical tomographic image reconstruction*', Inverse Problem, 19 (2003) 387-409.

[18] A.H. Hielschera, A.Y. Bluestone, G.S. Abdoulaev, A.D. Klose, J. Lasker, M. Stewart, U. Netz and J. Beuthan, '*Near-infrared diffuse optical tomography*', Disease Markers 18 (2002) 313–337, IOS Press

[19] Daqing Piao, Hamid Dehghani, Shudong Jiang, Subhadra Srinivasan, and Brian W. Pogue, '*Instrumentation for video-rate near-infrared diffuse optical tomography*', Review of Scientific instruments 76, 2005.

[20] A.M. Siegel, J.J.A.Marota and D. A. Boas, '*Design and evaluation of a continuous-wave diffuse optical tomography system*', Optics express, Vol.4, No.8, April 1999.

[21] Phaneendra K. Yalavarthy, Brian W. Pogue, Hamid Dehghani, Colin M. Carpenter, Shudong Jiang, and Keith D. Paulsen, '*Structural information within regularization matrices improves near infrared diffuse optical tomography*', Optics Express, Vol.15, No.13, June 25, 2007

[22] Brian W. Pogue, Keith D. Paulsen, Chris Abele, Howard Kaufman, '*Calibration of near-infrared frequency-domain tissue spectroscopy for absolute absorption coefficient quantitation in neonatal head-simulating phantoms*', Journal of Biomedical Optics, Vol.5, No.2, April 2000.

[23] Fabrizio Martelli and Giovanni Zaccanti, '*Calibration of scattering and absorption properties of a liquid diffusive medium at NIR wavelengths. CW method*', Optics Express / Vol. 15, No. 2 / January 22, 2007

[24] Sergio Fantini, Maria Angela Franceshini, Joshua B. Fishkin, Beniamino Barbieri, and Enrico Gratton, '*Quantitative determination of the absorption spectra of chromophores in strongly scattering media: a light-emitting-diode based technique*', Applied Optics, Vol.33, No.22, August, 1994.

[25] Steen J Madsen, Michael S Patterson and Brian C Wilson, '*The use of India ink as an optical absorber in tissue-simulating phantoms*' Phys. Med. Biol., 1992, Vol. 31, No 4, 985-993.

[26] Tuba Sahin, '*Near-Infrared Spectroscopy System for Monitoring Peripheral Vascular Disease*', Thesis for Master of Science, July 2003.

[27] Xueding Wang, Xueyi Xie, Geng Ku and Lihong V. Wang, '*Noninvasive imaging of hemoglobin concentration and oxygenation in the rat brain using high-resolution photoacoustic tomography*' Journal of Biomedical Optics 11(2), 024015 (March/April 2006)

[28] Chulhong Kim and Lihong V. Wang, '*Multi-optical-wavelength ultrasound-modulated optical tomography: a phantom study*', Optics Letters / Vol. 32, No. 16 / August 15, 2007

[29] Valentina Quaresima, Simona Sacco, Rocco Totaro and Marco Ferrari, '*Noninvasive measurement of cerebral hemoglobin oxygen saturation using two near infrared spectroscopy approaches*', Journal of Biomedical Optics / Vol. 5, No. 2 / April, 2000

[30] Xueding Wang, Geng Ku, malgorzata A. Wegiel, Darryl J. Bornhop, George Stoica and Lihong V. Wang,, '*Noninvasive photoacoustic angiography of animal brains in vivo with near-infrared light and an optical contrast agent*', Optics Letters / Vol. 29, No. 7 / April 1, 2004

[31] Xiaorong Xu, Wen Zhu, Vikram Padival, Mengna Xia, Xuefeng Cheng, Robin Bush, Linda Christenson, Tim Chan, Tim Doherty, and Angelo Iatridis, '*Validation of NIRS in measuring tissue hemoglobin concentration and oxygen saturation on Ex Vivo and isolated limb models*', Proc. of SPIE Vol. 4955 (2003) p.369-378

[32] Subhadra Srinivasan, Brian W. Pogue, Shudong Jian, Hamid Dehghani, Christine Kogel, Sandra Soho, Jennifer J. Gibson Tor D. Tosteson, Steven P.Poplack and Keith D. Paulsen. '*In Vivo hemoglobin and water concentrations, oxygen saturation, and scattering estimates from near-infrared breast tomography using spectral reconstruction*', Academic Radiology, Vol 13, No. 2, February 2006

APPENDEX A

MATLAB® Programs

Calib_auto_homo.m

```
%calculate source detector distances
[s_d_dist]=source_detector_dist;
back_inten=0;
%average the homogeneous data
a=imread('uni_back_1.tif');
phan_roi_ref=rot90(fliplr(a));
back_inten=double(min(min(a)));
[roi_s_min,roi_s_max,roi_d_min,roi_d_max]=find_ROI_auto_12mm_probe(phan_roi_ref, back_inten);

save roi_s_min roi_s_min
save roi_s_max roi_s_max
save roi_d_min roi_d_min
save roi_d_max roi_d_max
save back_inten back_inten

%take 64 ROIs
for source=1:8;
      s_pixel=roi_s_max(source)-roi_s_min(source)+1;
      for detector=1:8;
           d_pixel=roi_d_max(detector)-roi_d_min(detector)+1;
           data_roi(1:s_pixel,1:d_pixel)=phan_roi_ref(roi_s_min(source):roi_s_max(source),roi_d_min(dete
           ctor):roi_d_max(detector));
          data_aver(source,detector)=max(mean(data_roi,2));
      end
end

%reshape data
for source=1:8;
      data_aver_reshape(source, (1:(8+1-source)))=data_aver(source,source-1+(1:(8+1-source)));
      data_aver_reshape(source, ((8+2-source):8))=data_aver(source,1:(source-1));
end
for i=1:4
    nten_aver(i)=(mean(data_aver_reshape(:,i)-back_inten)+mean(data_aver_reshape(:,9-i)-back_inten))/2;
end
[p,q]=polyfit(s_d_dist, log(s_d_dist.*inten_aver),1);
%to obtain the intensity correction matrix for the entire 64 pixels.
for i=1:4;
inten_cal_matrix(1:8,i)=exp(p(1)*s_d_dist(i)+p(2))/s_d_dist(i)./(data_aver_reshape(1:8,i)-back_inten);
inten_cal_matrix(1:8,9-i)=exp(p(1)*s_d_dist(i)+p(2))/s_d_dist(i)./(data_aver_reshape(1:8,9-i)-back_inten);
end
save inten_cal_matrix inten_cal_matrix

%correct the intensity using the predetermined correction matrix
data_aver_reshape_cal=(data_aver_reshape-back_inten).*inten_cal_matrix;
%reshape to 240-point data
for i=1:8
      homo_auto_64((i-1)*8+(1:8))=data_aver_reshape_cal(i,1:8);
end

ff=homo_auto_64;
ff=ff';
ff(:,2)=8.5944;

save blo_sta.paa ff -ascii
```

Calib_auto_hete.m

```
for frame=1:1;
    a=imread([cat(2,'blo_sta_a_',num2str(frame),'.tif')]);
    data=rot90(fliplr(a));

    load roi_s_min
    load roi_s_max
    load roi_d_min
    load roi_d_max
    load back_inten

    for source=1:8;
        s_pixel=roi_s_max(source)-roi_s_min(source)+1;
        for detector=1:8;
            d_pixel=roi_d_max(detector)-roi_d_min(detector)+1;

data_roi(1:s_pixel,1:d_pixel)=data(roi_s_min(source):roi_s_max(source),roi_d_min(detector):roi_d_max(d
etector));
            data_aver(source,detector)=max(mean(data_roi,2));
        end
    end

%reshape data
    for source=1:8;
        data_aver_reshape(source, (1:(8+1-source)))=data_aver(source,source-1+(1:(8+1-source)));
        data_aver_reshape(source, ((8+2-source):8))=data_aver(source,1:(source-1));
    end
%correct the intensity using the predetermined correction matrix
    data_aver_reshape_cal=(data_aver_reshape-back_inten).*inten_cal_matrix;
%reshape to 240-point data
    for i=1:8
        hete_auto_64((i-1)*8+(1:8))=data_aver_reshape_cal(i,1:8);
    end

    ff=hete_auto_64;
    ff=ff';
    ff(:,2)=8.5944;
    save blo_sta_780nm.paa ff -ascii

    eval(['save c:\research\data\dot\spread_encoding\Blood\blood_080110_whole_test_0.5\blo_sta_'
    num2str(frame) '.paa ff -ascii'])
    save blo_sta_780nm.paa ff -ascii

    calibrate_cw_endo('blo_sta_080110_780nm.paa','blo_sta_780nm.paa','probe_id6_dep15_int05p',1,'rec
    on_mesh','hete_cal.paa',100,10);

    close all
    [mesh,pj_error]=reconstruct_cw_endo('recon_mesh',[30 30],0,'hete_cal.paa',10,10,'recon_image',-1);
    eval(['mua_hete_' num2str(frame) '=mesh.mua;'])
    eval(['save c:\research\data\dot\spread_encoding\Blood\blood_080110_whole_test_0.5\blo_sta_'
    num2str(frame) ' mua_hete_' num2str(frame)]);
    frame
end
```

Source_detector_dist.m

```
function [s_d_dist]=source_detector_dist
r_phan=6.5; %phantom diameter
for i=1:8      % find source coordinates
       s_x(i)=-r_phan*cos((i-1)*pi/4);
       s_y(i)=r_phan*sin((i-1)*pi/4);
end

for i=1:8      %find detector coordinates
       d_x(i)=-r_phan*cos((i-1)*pi/4+pi/8);
       d_y(i)=r_phan*sin((i-1)*pi/4+pi/8);
end

for i=1:4
       s_d_dist(i)=sqrt((s_x(1)-d_x(i))^2+(s_y(1)-d_y(i))^2);
End
```

Calibrate_cw_endo.m

```
function calibrate_cw_endo(homog_data,...
                           anom_data,...
                           mesh_fn_homog,...
                           mus,...
                           mesh_op, ...
                           data_op,...
                           frequency,...
                           iteration)
% load mesh for homogeneuos phantom
mesh_homog = load_mesh_endo(mesh_fn_homog);
mesh_anom=mesh_homog;
% load anomaly data
paa_anom      = load(anom_data);
% set log amplitude
paa_anom(:,1) = log(paa_anom(:,1));
% we have no phase data, so just create some based on the given value
mesh_anom.mus(:) = mus;
foo = femdata_endo('foo_anom',100,mesh_anom);
paa_anom(:,2) = foo.phase;
clear foo

paa_homog    = load(homog_data);
% set log amplitude
paa_homog(:,1) = log(paa_homog(:,1));
% we have no phase data, so set it same as homog
paa_homog(:,2) = paa_anom(:,2);
% Calculate global mua and mus plus offsets for phantom data
[mua_h,mus_h,lnI_h,phase_h,data_h_fem] = fit_data_endo('foo_homog',...
                                    mesh_homog,...
                                    paa_homog,...
                                    frequency,...
                                    iteration);
data_h_fem(:,1) = log(data_h_fem(:,1));
% Calculate global mua and mus plus offsets for patient data
[mua_a,mus_a,lnI_a,phase_a,data_a_fem] = fit_data_endo('foo_anom',...
                                    mesh_anom,...
                                    paa_anom,...
                                    frequency,...
                                    iteration);
data_a_fem(:,1) = log(data_a_fem(:,1));
% calculate offsets between modelled homogenous and measured
paa_cal = paa_anom - ((paa_homog - data_h_fem));
paa_cal(:,1) = paa_cal(:,1) - (lnI_a-lnI_h);
paa_cal(:,1) = exp(paa_cal(:,1));
paa_cal(:,2) = 0;
% write caliberated data out
mysave(data_op,paa_cal);
% set mesh values for global calculated patient values
mesh_anom.mua(:) = mua_a;
mesh_anom.mus(:) = mus_a;
mesh_anom.kappa = 1./(3*(mesh_anom.mua+mesh_anom.mus));
save_mesh(mesh_anom,mesh_op);
delete *foo*
```

Femdata_endo.m

```
function [data,mesh]=femdata_endo(fil_name,frequency,param)

% load mesh data
if nargin == 2
   mesh = load_mesh_endo(fil_name);
elseif nargin == 3
   mesh = param;
   clear param;
end

% modulation frequency
omega = 2*pi*frequency*1e6;

% Create FEM matricex
if mesh.dimension == 2
   [i,j,s] = gen_matrices_2d(mesh.nodes(:,1:2),...
                             sort(mesh.elements')', ...
                             mesh.bndvtx,...
                             mesh.mua,...
                             mesh.kappa,...
                             mesh.ksi,...
                             mesh.c,...
                             omega);
elseif mesh.dimension ==3
   [i,j,s] = gen_matrices_3d(mesh.nodes,...
                             sort(mesh.elements')', ...
                             mesh.bndvtx,...
                             mesh.mua,...
                             mesh.kappa,...
                             mesh.ksi,...
                             mesh.c,...
                             omega);
end
junk = length(find(i==0));
MASS = sparse(i(1:end-junk),j(1:end-junk),s(1:end-junk));
clear junk i j s omega

if exist([fil_name '.ident']) ~= 0
   disp('Modifying for refractive index')
   mesh.ident = load([fil_name '.ident']);
   M = bound_int(MASS,mesh);
   MASS = M;
   clear M
end

%calculate source vector
[n_nodes,junk]=size(mesh.nodes);
[n_source,junk]=size(mesh.source);
qvec = spalloc(n_nodes,n_source,n_source*100);
if mesh.dimension == 2
   for i = 1 : n_source
      qvec(:,i) = gen_source(mesh.nodes(:,1:2),...
                             sort(mesh.elements')',...
                             mesh.dimension,...
```

```
                        mesh.source(i,1:2),...
                        3);
    end
elseif mesh.dimension == 3
    for i = 1 : n_source
        qvec(:,i) = gen_source(mesh.nodes,...
                        sort(mesh.elements')',...
                        mesh.dimension,...
                        mesh.source(i,:),...
                        3);
    end
end

clear junk i nnodes nsource;

% Catch zero frequency (CW) here
if frequency == 0
    MASS = real(MASS);
    qvec = real(qvec);
end

% Calculate field for all sources
[data.phi]=get_field(MASS,mesh,qvec);
clear qvec;

% Calculate boundary data
[data.complex]=get_boundary_data(mesh,data.phi);

% Map complex data to amplitude and phase
data.amplitude = abs(data.complex);
data.phase = atan2(imag(data.complex),...
                real(data.complex));
data.phase(find(data.phase<0)) = data.phase(find(data.phase<0)) + (2*pi);
data.phase = data.phase*180/pi;
data.paa = [data.amplitude data.phase];
```

Reconstruct_cw_endo.m

```
function [fwd_mesh,pj_error] = reconstruct_cw_endo(fwd_fn,...
                                    recon_basis,...
                                    frequency,...
                                    data_fn,...
                                    iteration,...
                                    lambda,...
                                    output_fn,...
                                    filter_n)
tic;
% load fine mesh for fwd solve
fwd_mesh = load_mesh_endo(fwd_fn);

if ischar(recon_basis)
   recon_mesh = load_mesh_endo(recon_basis);
   [fwd_mesh.fine2coarse,...
    recon_mesh.coarse2fine] = second_mesh_basis(fwd_mesh,recon_mesh);
else
   [fwd_mesh.fine2coarse,recon_mesh] = pixel_basis(recon_basis,fwd_mesh);
end

% read data
anom = load(data_fn);
anom = log(anom(:,1));
% Initiate projection error
pj_error = [];
% Initiate log file
fid_log = fopen([output_fn '.log'],'w');
fprintf(fid_log,'Absoprtion reconstruction from amplitude only\n');
fprintf(fid_log,'Forward Mesh      = %s\n',fwd_fn);
if ischar(recon_basis)
   fprintf(fid_log,'Basis             = %s\n',recon_basis);
else
   fprintf(fid_log,'Basis             = %s\n',num2str(recon_basis));
end
fprintf(fid_log,'Frequency         = %f MHz\n',frequency);
fprintf(fid_log,'Data File         = %s\n',data_fn);
fprintf(fid_log,'Initial Reg       = %d\n',lambda);
fprintf(fid_log,'Filter            = %d\n',filter_n);
fprintf(fid_log,'Output Files      = %s_mua.sol\n',output_fn);
fprintf(fid_log,'                  = %s_mus.sol\n',output_fn);

for it = 1 : iteration
   % Calculate jacobian
   [J,data]=jacobian(fwd_fn,frequency,fwd_mesh);
    % Read reference data
   clear ref;
   ref(:,1) = log(data.amplitude);
   data_diff = (anom-ref);

   pj_error = [pj_error sum((anom-ref).^2)];
   disp('--------------------------------');
   disp(['Iteration Number          = ' num2str(it)]);
   disp(['Projection error          = ' num2str(pj_error(end))]);
```

```
  fprintf(fid_log,'--------------------------------\n');
  fprintf(fid_log,'Iteration Number                = %d\n',it);
  fprintf(fid_log,'Projection error                = %f\n',pj_error(end));

  if it ~= 1
     p = (pj_error(end-1)-pj_error(end))*100/pj_error(end-1);
     disp(['Projection error change      = ' num2str(p) '%']);
     fprintf(fid_log,'Projection error change      = %f %%\n',p);
     if (p) <= 2
        disp('---------------------------------');
        disp('STOPPING CRITERIA REACHED');
        fprintf(fid_log,'--------------------------------\n');
        fprintf(fid_log,'STOPPING CRITERIA REACHED\n');
      break
     end
  end

  % Interpolate onto recon mesh
  [J,recon_mesh] = interpolatef2r(fwd_mesh,recon_mesh,J.complete);
  % build hessian
  [nrow,ncol]=size(J);
  Hess = zeros(nrow);
  Hess = (J*J');
  % initailize temp Hess, data and mesh, incase PJ increases.
  Hess_tmp = Hess;
  mesh_tmp = recon_mesh;
  data_tmp = data_diff;
  % Add regularization
  if it ~= 1
     lambda = lambda./10^0.25;
  end

  reg = eye(nrow).*lambda*max(diag(Hess));
  disp(['Amp Regularization           = ' num2str(reg(1,1))]);
  fprintf(fid_log,'Amp Regularization           = %f\n',reg(1,1));

 Hess = Hess+reg;
  % Calculate update
  foo = J'*(Hess\data_diff);
  % Update values
  recon_mesh.mua = recon_mesh.mua + foo;
  clear foo Hess Hess_norm tmp data_diff G
  % Interpolate optical properties to fine mesh
  [fwd_mesh,recon_mesh] = interpolatep2f(fwd_mesh,recon_mesh);
  % We dont like -ve mua or mus! so if this happens, terminate
  if (any(fwd_mesh.mua<0) | any(fwd_mesh.mus<0))
     disp('---------------------------------');
     disp('-ve mua or mus calculated...not saving solution');
     fprintf(fid_log,'--------------------------------\n');
     fprintf(fid_log,'STOPPING CRITERIA REACHED\n');
     break
  end

% Filtering if needed!
  if filter_n > 1
     fwd_mesh = mean_filter(fwd_mesh,abs(filter_n));
```

```
    elseif filter_n < 1
        fwd_mesh = median_filter(fwd_mesh,abs(filter_n));
    end

    if it == 1
        fid = fopen([output_fn '_mua.sol'],'w');
    else
        fid = fopen([output_fn '_mua.sol'],'a');
    end
    fprintf(fid,'solution %g ',it);
    fprintf(fid,'-size=%g ',length(fwd_mesh.nodes));
    fprintf(fid,'-components=1 ');
    fprintf(fid,'-type=nodal\n');
    fprintf(fid,'%f ',fwd_mesh.mua);
    fprintf(fid,'\n');
    fclose(fid);

    if it == 1
        fid = fopen([output_fn '_mus.sol'],'w');
    else
        fid = fopen([output_fn '_mus.sol'],'a');
    end
    fprintf(fid,'solution %g ',it);
    fprintf(fid,'-size=%g ',length(fwd_mesh.nodes));
    fprintf(fid,'-components=1 ');
    fprintf(fid,'-type=nodal\n');
    fprintf(fid,'%f ',fwd_mesh.mus);
    fprintf(fid,'\n');
    fclose(fid);
end

% close log file!
time = toc;
fprintf(fid_log,'Computation TimeRegularization = %f\n',time);
fclose(fid_log);

function [val_int,recon_mesh] = interpolatef2r(fwd_mesh,recon_mesh,val)

NNC = size(recon_mesh.nodes,1);
NNF = size(fwd_mesh.nodes,1);
NROW = size(val,1);
val_int = zeros(NROW,NNC);

for i = 1 : NNF
    if recon_mesh.coarse2fine(i,1) ~= 0
        val_int(:,recon_mesh.elements(recon_mesh.coarse2fine(i,1),:)) = ...
        val_int(:,recon_mesh.elements(recon_mesh.coarse2fine(i,1),:)) + ...
        val(:,i)*recon_mesh.coarse2fine(i,2:end);
    elseif recon_mesh.coarse2fine(i,1) == 0
        dist = distance(fwd_mesh.nodes,fwd_mesh.bndvtx,recon_mesh.nodes(i,:));
        mindist = find(dist==min(dist));
        mindist = mindist(1);
        val_int(:,i) = val(:,mindist);
    end
end
for i = 1 : NNC
```

```
    if fwd_mesh.fine2coarse(i,1) ~= 0
        recon_mesh.mua(i,1) = (fwd_mesh.fine2coarse(i,2:end) * ...
        fwd_mesh.mua(fwd_mesh.elements(fwd_mesh.fine2coarse(i,1),:)));
        recon_mesh.mus(i,1) = (fwd_mesh.fine2coarse(i,2:end) * ...
        fwd_mesh.mus(fwd_mesh.elements(fwd_mesh.fine2coarse(i,1),:)));
        recon_mesh.kappa(i,1) = (fwd_mesh.fine2coarse(i,2:end) * ...
        fwd_mesh.kappa(fwd_mesh.elements(fwd_mesh.fine2coarse(i,1),:)));
        recon_mesh.region(i,1) = ...
        median(fwd_mesh.region(fwd_mesh.elements(fwd_mesh.fine2coarse(i,1),:)));
    elseif fwd_mesh.fine2coarse(i,1) == 0
        dist = distance(fwd_mesh.nodes,...
                        fwd_mesh.bndvtx,...
                        [recon_mesh.nodes(i,1:2) 0]);
        mindist = find(dist==min(dist));
        mindist = mindist(1);
        recon_mesh.mua(i,1) = fwd_mesh.mua(mindist);
        recon_mesh.mus(i,1) = fwd_mesh.mus(mindist);
        recon_mesh.kappa(i,1) = fwd_mesh.kappa(mindist);
        recon_mesh.region(i,1) = fwd_mesh.region(mindist);
    end
end

function [fwd_mesh,recon_mesh] = interpolatep2f(fwd_mesh,recon_mesh)

for i = 1 : length(fwd_mesh.nodes)
    fwd_mesh.mua(i,1) = ...
          (recon_mesh.coarse2fine(i,2:end) * ...
           recon_mesh.mua(recon_mesh.elements(recon_mesh.coarse2fine(i,1),:)));
    fwd_mesh.kappa(i,1) = ...
          (recon_mesh.coarse2fine(i,2:end) * ...
           recon_mesh.kappa(recon_mesh.elements(recon_mesh.coarse2fine(i,1),:)));
    fwd_mesh.mus(i,1) = ...
          (recon_mesh.coarse2fine(i,2:end) * ...
           recon_mesh.mus(recon_mesh.elements(recon_mesh.coarse2fine(i,1),:)));
end
```

VITA

HAO XIE

Candidate for the Degree of

Master of Science

Thesis: DUAL-SPECTRAL ENDOSCOPIC NEAR-INFRARED OPTICAL TOMOGRAPHY FOR ASSESSMENT OF HEMOGLOBIN CONCENTRATION AND OXYGEN SATURATION

Major Field: Biomedical Engineering

Biographical:

Personal Data:

Education: Graduated from Beihang High School, Beijing, China in May 1993; received Bachelor of Science degree in Electrical engineering from North China Electrical Power University, Beijing, China in June 1997. Completed the requirements for the Master of Science degree with a major in Electrical Engineering at School of Electrical and Computer Engineering, Oklahoma State University, Stillwater, Oklahoma in July, 2008.

Experience: Employed by Oklahoma State University, School of Electrical and Computer Engineering as a graduate research assistant; Oklahoma State University, School of Electrical and Computer Engineering, 2005-2008. Employed by China Electrical Power Research Institute as an electrical engineer; 1997-2005.

Professional Memberships: SPIE (student member)

Name: HAO XIE Date of Degree: July, 2008

Institution: Oklahoma State University Location: Stillwater, Oklahoma

Title of Study: DUAL-SPECTRAL ENDOSCOPIC NEAR-INFRARED OPTICAL TOMOGRAPHY FOR ASSESSMENT OF HEMOGLOBIN CONCENTRATION AND OXYGEN SATURATION

Pages in Study: 67 Candidate for the Degree of Master of Science

Major Field: Electrical Engineering

Scope and Method of Study: Near-infrared diffuse optical tomography (NIR-DOT) can provide high intrinsic contrast images of the human tissue. To imaging internal organ like prostate, it is necessary to develop endoscopic mode NIR-DOT system. Furthermore, due to the different optical diffuse coefficients of the oxygenated and deoxygenated hemoglobin in the near infrared band, the total hemoglobin concentration (HbT) and the oxygen saturation of the blood (StO2) can be quantitatively estimated by implementing dual-spectral detection into endoscopic mode near-infrared diffuse optical tomography system.

Findings and Conclusions: In this project, the phantom study and the blood test were performed; the preliminary results showed that by implementing dual-spectral detection into the endoscopic probe, the near-infrared optical tomography imaging system could reveal the absorption coefficient changes of the heterogeneous objects and the blood StO2 changes.

ADVISER'S APPROVAL: Daqing. Piao